

Ab Initio Superionic-Liquid Phase Diagram of $\text{Fe}_{1-x}\text{O}_x$ under Earth's Inner Core Conditions

Zepeng Wu¹, Chen Gao¹, Feng Zhang,² Shunqing Wu^{1,*}, Kai-Ming Ho,²
Renata M. Wentzcovitch^{3,4,5,6,†}, and Yang Sun^{1,‡}

¹*Department of Physics, Xiamen University, Xiamen 361005, China*

²*Department of Physics and Astronomy, Iowa State University, Ames, Iowa 50011, USA*

³*Department of Applied Physics and Applied Mathematics, Columbia University, New York, New York 10027, USA*

⁴*Department of Earth and Environmental Sciences, Columbia University, New York, New York 10027, USA*

⁵*Lamont-Doherty Earth Observatory, Columbia University, Palisades, New York 10964, USA*

⁶*Data Science Institute, Columbia University, New York, New York 10027, USA*



(Received 8 August 2024; accepted 14 November 2025; published 6 January 2026)

The superionic state is a phase of matter in which liquidlike ionic mobility coexists with a solid crystalline lattice. Recently identified in Earth's inner core (IC), this state has attracted considerable attention for its unique kinetic behavior and geophysical implications. However, the *ab initio* phase diagram describing the equilibrium between the superionic phase and the liquid solution under core conditions remains largely unexplored. Here, we present a thermodynamic approach to compute the Gibbs free energy and construct the *ab initio* superionic-liquid phase diagram for the $\text{Fe}_{1-x}\text{O}_x$ system under IC conditions. We find that oxygen forms superionic states in both hcp and bcc Fe phases, with a pronounced influence on cooperative diffusion of iron in the bcc lattice. The stability fields of these superionic phases are sensitive to oxygen stoichiometry. The presence of superionic states leads to a higher oxygen concentration in the IC than previously estimated. Our Letter establishes a framework for investigating superionic-liquid equilibria under extreme conditions.

DOI: 10.1103/37nh-5ws8

Superionicity is a unique state where materials exhibit liquid-like mobility within a crystal lattice, drawing great interest in various scientific and industrial fields. Under ambient conditions, this property is crucial for solid electrolytes vital for next-generation all-solid-state batteries [1,2]. At extremely high pressures and temperatures, solid phases can transform into superionic states [3–7], as is believed to occur in minerals of Earth's deep mantle [8–10], as well as in ice and ammonia within the mantles of Uranus and Neptune [11–17]. Recent simulations reveal that light elements like oxygen, hydrogen, and carbon can become superionic in hexagonal close-packed (hcp) iron under Earth's inner core (IC) conditions [18]. The kinetic behavior of the superionic state is proposed to cause the anisotropic seismic characteristics of the IC [19]. However, the stability field of the superionic state in the IC remains unclear. The phase competition between hcp and body-centered cubic (bcc) iron under IC conditions has long been debated [20,21]. While recent studies suggest hcp as the stable phase [22,23], it is uncertain if superionic states can emerge in bcc Fe-light element alloys and affect their stability relative to superionic hcp alloys under IC

conditions. As the compositions of light elements were determined based on the solid solution models of the hcp phase [24–26], superionic solutions could alter our understanding of light element partitioning between the solid IC and the liquid outer core. Thus, determining the thermodynamic stability of superionic phases, especially their equilibrium with liquid solutions at the inner core boundary (ICB), is crucial not only for fundamental physics in the novel state but also for constraining the core's structure and chemical composition, which are vital for understanding the Earth's deep interior [20,27].

Despite its importance, exploring the stability of the superionic phase in the IC is challenging. Experimental observation of superionicity in Fe alloys is lacking due to the difficulty of detecting this state under IC conditions. Theoretical studies of phase competition among liquid, superionic, and solid phases are scarce, as calculating the free energy of the superionic state is highly non-trivial [28]. In the case of superionic ice, several attempts have been proposed to compute its free energy. A typical method is based on thermodynamic integration (TI), which provides the difference in free energy between the superionic phase and a reference model for which absolute free energy is known as *a priori*. Although TI is accurate, finding a suitable reference for the superionic phase is difficult. Wilson *et al.* proposed using noninteracting harmonic

*Contact author: wsq@xmu.edu.cn

†Contact author: rmw2150@columbia.edu

‡Contact author: yangsun@xmu.edu.cn

oscillators and an ideal gas as a superionic reference [29]. However, this model suffers from the problem of particle overlap due to the lack of interactions between solidlike and liquidlike particles [30]. Cheng *et al.* used machine learning interatomic potentials to simulate the superionic and liquid coexistence for stoichiometric ice phases, providing melting curves for superionic ice [14]. While simulations of coexisting phases are sufficient to establish phase equilibria for stoichiometric systems such as H₂O, as we will demonstrate later, direct calculations of the absolute free energy for the liquid and superionic phases are necessary to obtain a complete phase diagram for the nonstoichiometric Fe_{1-x}O_x system. Moreover, classical simulations strongly depend on the accuracy of the interatomic potentials, even trained by machine learning techniques [31]. An approach that eliminates dependence on interatomic potential accuracy and enables the determination of the superionic phase's free energy at the *ab initio* level remains desirable. In principle, the interatomic potential can serve as a reference model for computing the *ab initio* Gibbs free energy of the superionic state in TI. A similar method was recently developed to determine the melting temperatures and relative free energies of pure Fe phases under IC conditions [22], showing that classical simulations provide a suitable reference for *ab initio* calculations using classical to *ab initio* thermodynamic integration (CATI) and free-energy perturbation (FEP) methods [22,32]. While this method is relatively straightforward for systems with constant stoichiometry like H₂O or Fe, it becomes complex for nonstoichiometric solutions where the chemical potential of solute atoms in liquid and superionic phases is critical.

In this Letter, we develop a scheme to calculate the *ab initio* superionic-liquid phase diagram for the nonstoichiometric Fe_{1-x}O_x system under conditions close to Earth's ICB, considering the superionic state in both hcp and bcc phases. We first construct a Fe-O interatomic potential to simulate the coexistence of superionic and liquid phases in Fe_{1-x}O_x systems using large-scale, long-timescale molecular dynamics (MD) simulations, which provide solidus and liquidus curves. Based on thermodynamic relations, we show that the *absolute* Gibbs free energy of the superionic phase can be computed without any assumption. Using CATI and FEP methods, we obtain the *ab initio* Gibbs free energy of both liquid and superionic phases from the interatomic-potential reference. By introducing the realistic physical reference for the superionic state, we eliminate the particle-overlap problem in previous thermodynamic integration calculations [29,30]. The framework (Supplemental Material Fig. S1 [33]) allows us to construct a superionic-liquid phase diagram with *ab initio* accuracy. We elucidate phase competition between superionic hcp and bcc structures and assess the impact of the superionic state on O partitioning between inner and outer cores.

Effect of superionic oxygen on Fe's cooperative motion—The key feature of the superionic Fe_{1-x}O_x alloy is the O diffusion in the crystalline lattice. Based on the AIMD

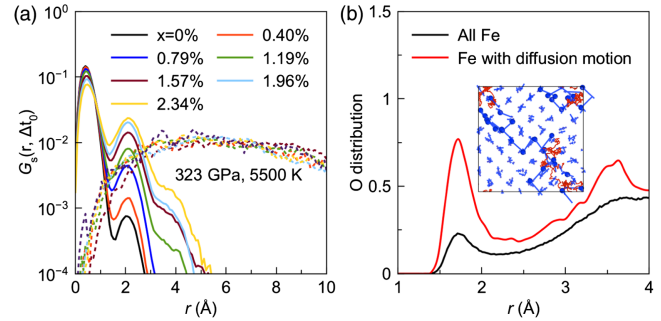


FIG. 1. The effect of superionic O on the Fe's cooperative diffusion in bcc. (a) The van Hove self-correlation function for Fe_{1-x}O_x bcc phases at 323 GPa and 5500 K. (b) The radial distribution function of O surrounding Fe atoms. Red line is for the Fe exhibiting cooperative diffusion motion. The data are collected in 1.5 ps prior to the completion of Fe's cooperative diffusion motion. The inset shows the trajectory of Fe's cooperative diffusion motion (blue) and O's superionic motions (red). The Fe atoms exhibiting only vibrational motions are reduced in size for clarity.

simulation, O exhibits superionic behavior in both hcp and bcc Fe under ICB conditions. It shows a similar mean squared displacement (MSD) in hcp, bcc, and liquid Fe phases at 323 GPa and 5500 K, conditions close to those at ICB (Supplemental Material Fig. S4 [33]). In the bcc lattice, Fe atoms exhibit cooperative diffusion motion under IC conditions, where atoms move in a stringlike manner among crystalline sites [21,58]. We quantify the Fe's motion using the van Hove self-correlation function $G_s(r, \Delta t) = (1/N) \langle \sum_{i=1}^N \delta(\vec{r} + \vec{r}_i(0) - \vec{r}_i(\Delta t)) \rangle$, where Δt is chosen to be 6 ps, which can well distinguish the vibrational motion from the cooperative diffusion motion. As shown in Fig. 1(a), the second peak of Fe's van Hove self-correlation function at 2.1 Å systematically increases with rising oxygen concentration. This peak corresponds to Fe's cooperative motion with its nearest neighboring Fe atom. Moreover, a third peak at 3.8 Å emerges when x_O exceeds 1.19%, suggesting multiple cooperative motions within the time period. Thus, with higher oxygen concentrations, Fe's diffusion motion becomes more pronounced. Figure 1(b) shows that Fe atoms exhibiting cooperative motion have more oxygen neighbors than the average distribution. The trajectory in Fig. 1(b) also provides a clear visualization of this phenomenon. Thus, superionic oxygen enhances Fe's cooperative diffusion motion in the bcc phase under IC conditions. This can be attributed to the fact that O enhances the tendency of Fe atoms to deviate from their crystalline sites, as indicated by the phonon instability analysis in the bcc lattice (Supplemental Material Note 1 [33]).

Superionic-liquid coexistence—Because *ab initio* MD simulation is highly limited by the time and length scales, we employ classical MD simulations to study the stability of superionic phases coexisting with liquid. We developed a Fe-O interatomic potential using the embedded-atom method (EAM) [59], which can simulate the superionic

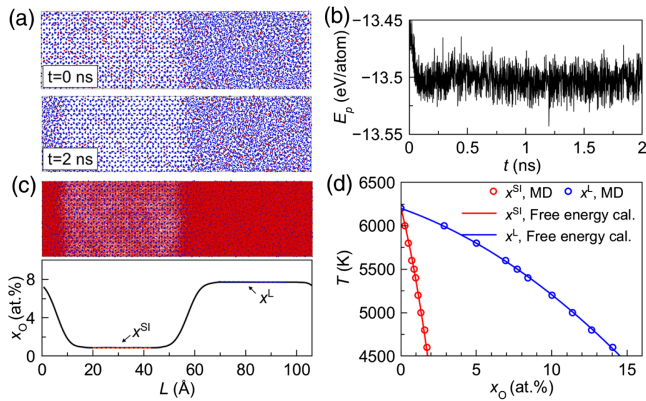


FIG. 2. Superionic-liquid coexistence simulations of $\text{Fe}_{1-x}\text{O}_x$ solution. (a) Initial and final configurations the coexistence simulation at 323 GPa and 5500 K. The blue and red dots represent Fe and O atoms, respectively. (b) Potential energy as a function of time in the simulation. (c) O trajectory in last 1 ns. The lower panel shows the averaged O composition along the direction perpendicular to the interface. (d) The phase diagram by classical MD simulation at 323 GPa. The circles are from direct superionic-liquid coexistence simulations. The lines are from free energy calculations.

state in both hcp and bcc lattices without any instability under ICB conditions. The MSD from classical MD align qualitatively well with *ab initio* data (Supplemental Material Note 2 [33]). To simulate the superionic hcp-liquid coexistence, we construct a two-phase model with an hcp-liquid interface using 12 288 Fe atoms and randomly distributed O atoms for various O compositions. After MD simulations, O composition decreases in the hcp phase as shown in Fig. 2(a). The system reaches equilibrium at around 100 ps, as indicated by the energy change in Fig. 2(b). With a long simulation time of 2 ns, O atoms diffused throughout the simulation cell, providing sufficient data to compute their equilibrium composition in the hcp and liquid phases in Fig. 2(c). The O composition in the superionic phase (x_C^{SI}) is significantly lower than that in the liquid phase (x_C^L). Tests with larger system sizes suggest the current size is sufficient to obtain converged results (Supplemental Material Fig. S8 [33]). Similar simulations across temperatures from 4600–6000 K at the same pressure yielded temperature-dependent x_C^{SI} and x_C^L , representing the superionic hcp solidus and liquidus lines in Fig. 2(d).

Based on the thermodynamic relations, when $\text{Fe}_{1-x}\text{O}_x$ superionic solution coexists in equilibrium with the liquid solution, it satisfies the equilibrium condition,

$$G_C^{SI}(x_{C0}^{SI}) = G_C^L(x_{C0}^L) - (x_{C0}^L - x_{C0}^{SI}) \frac{\partial G_C^L(x)}{\partial x} \Big|_{x=x_{C0}^L}, \quad (1)$$

where $G_C^L(x_{C0}^L)$ and $G_C^{SI}(x_{C0}^{SI})$ are absolute Gibbs free energies of liquid and superionic phases with O compositions of x_{C0}^L and x_{C0}^{SI} , respectively. The detailed derivations of

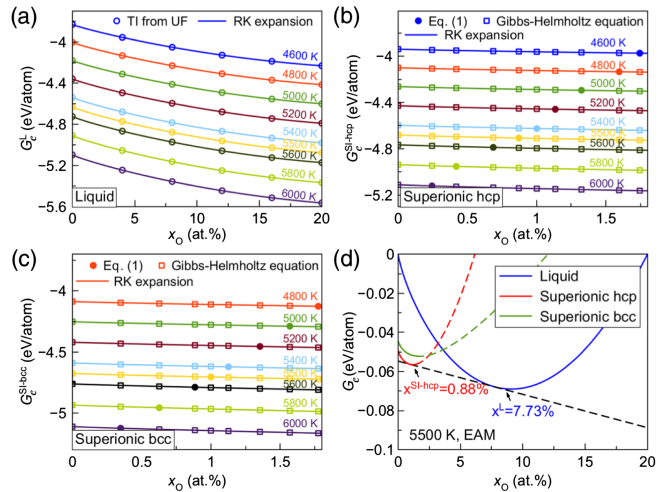


FIG. 3. (a) The composition-dependent Gibbs free energy of liquid solutions with EAM potential at 323 GPa. (b) The composition-dependent Gibbs free energy of superionic hcp solutions. The solid circles are computed based on the superionic-liquid equilibrium condition in Eq. (1). The open squares are computed based on the Gibbs-Helmholtz equation and the values of the solid circles. The solid lines represent the fitting with the RK expansion. (c) The composition-dependent Gibbs free energy of superionic bcc solutions. (d) The relative Gibbs free energy for liquid and superionic solutions at 323 GPa and 5500 K from EAM potential. The solid (dashed) line indicates the interpolated (extrapolated) results using RK expansion. The dashed line is the common tangent between liquid and superionic hcp data, defining solidus and liquidus compositions. The data are referenced to 0% and 20% liquid free energy for better visualization.

Eq. (1) are presented in End Matter. Since the MD simulation in Fig. 2(d) provides x_{C0}^L and x_{C0}^{SI} at various temperatures T_0 , Eq. (1) can be employed to compute the Gibbs free energy of the superionic phase $G_C^{SI}(x_{C0}^{SI}, T_0)$, provided the liquid's Gibbs free energy $G_C^L(x, T_0)$ is known. The nonequilibrium TI method was employed to compute the Helmholtz free energy for the liquid solutions (Supplemental Material Note 3 [33]). A series of free energy calculations for a liquid solution are performed across the O composition range of 0–20 at.%, with the compositions spaced equally, at various temperatures in Fig. 3(a). We find these liquid's free energy data can be well described by the regular solution model using the Redlich-Kister (RK) expansion [60] as

$$G(x, T_0) = G^{Fe}(T_0) + ax + x(1-x) \sum_{k=0}^{n_k} L_k (2x-1)^k + k_B T_0 [x \ln x + (1-x) \ln(1-x)], \quad (2)$$

where $G^{Fe}(T_0)$ is the Gibbs free energy of pure Fe. a and L_k are the fitting parameters. It only requires two RK terms ($k=0$ and 1) to fit the liquid's free energy data, achieving fitting errors of less than 0.1 meV/atom at all temperatures studied.

Based on Eq. (1) and $G_C^L(x, T_0)$, we can compute $G_C^{SI}(x_{C0}^{SI}, T_0)$ for each $(x_{C0}^{SI}, x_{C0}^L, T_0)$ combination obtained

from superionic-liquid coexistence simulations in Fig. 2(d). This results in sparse Gibbs free energy data for the superionic hcp state at a few temperatures, marked as solid circles in Fig. 3(b). We then extend these data to a broader temperature range using the Gibbs-Helmholtz equation,

$$G(x_0, T) = \frac{T}{T_0} G(x_0, T_0) - T \int_{T_0}^T \frac{H(x_0, T)}{T^2} dT, \quad (3)$$

where $H(x_0, T)$ is the temperature-dependent enthalpy with a specific O composition of x_0 obtained from MD simulations. Temperature-dependent $G_C^{SI}(x_{C0}^{SI}, T)$ are computed with Eq. (3) for different x_{C0}^{SI} and plotted as a function of compositions in Fig. 3(b). The free energy of the superionic phase can also be well fitted by Eq. (2) (Supplemental Material Note 4 [33]) using only one RK term ($k = 0$) to achieve fitting errors of less than 0.2 meV/atom (Supplemental Material Fig. S9 [33]).

With the absolute Gibbs free energy for both liquid and superionic solutions across various compositions and temperatures, the common tangent line can be computed to get the solidus and liquidus curves. Figure 3(d) shows the common tangent lines computed between $G_C^{SI-hcp}(x)$ and $G_C^L(x)$ curves at 5500 K, which resulted in intersections at $x_{C0}^{SI-hcp} = 0.88\%$ and $x_{C0}^L = 7.73\%$. These values are consistent with the equilibrium compositions of $x_{C0}^{SI-hcp} = 0.87\%$ and $x_{C0}^L = 7.70\%$ obtained from superionic hcp-liquid coexistence simulations under the same pressure and temperature conditions shown in Fig. 2(c). More free energy data and their common tangent lines at other temperatures are shown in Supplemental Material Fig. S14 [33]. The superionic hcp solidus and liquidus curves computed from the free energy calculations are compared with those from coexistence simulations in Fig. 2(d). Both methods result in a consistent superionic-liquid phase diagram, validating each other.

Using Eqs. (1)–(3), we repeated the calculations for the superionic bcc phase. The temperature-dependent free energies of superionic bcc are shown in Fig. 3(c). The solidus and liquidus curves of superionic bcc are shown in Fig. S15 [33]. Figure 3(d) and Supplemental Material Fig. S14 [33] compare the relative free energy among liquid, superionic bcc, and superionic hcp phases at 5500 K. These data suggest that the superionic bcc is metastable compared to the superionic hcp phase when the O composition is small. When the O composition is greater than ~ 3 at.%, the superionic bcc becomes more stable than superionic hcp in $\text{Fe}_{1-x}\text{O}_x$.

Ab initio Gibbs free energy of superionic phases—We have obtained the absolute Gibbs free energy, G_C , of the liquid and superionic solutions for the EAM system. Using the classical EAM system as the reference state, we can perform CATI [22,61] to compute the *ab initio* Gibbs free energy G_A by

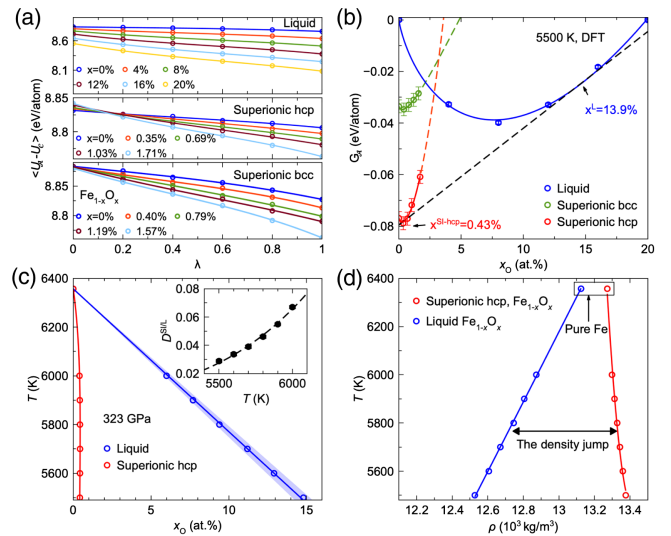


FIG. 4. *Ab initio* phase diagram of superionic and liquid $\text{Fe}_{1-x}\text{O}_x$ solutions. (a) The energy differences in the TI calculation from the classical to the *ab initio* system. The lines are the third-order polynomial fitting. (b) The relative *ab initio* Gibbs free energy for liquid, superionic hcp, and superionic bcc solutions. The solid and dashed lines indicate the interpolated and extrapolated results using RK expansion, respectively. The black dashed line is the common tangent line. (c) The superionic-liquid phase diagram of the $\text{Fe}_{1-x}\text{O}_x$ superionic-liquid system at the *ab initio* level at 323 GPa. The inset shows the temperature dependent partition coefficient, $D^{SI/L} = x_A^{SI}/x_A^L$. The shaded areas represent the uncertainty ranges of x^L and x^{SI} . (d) Density of superionic hcp and liquid $\text{Fe}_{1-x}\text{O}_x$ under the equilibrium composition at different temperatures.

$$G_A = G_C + f_{PV} + f_{TI}, \quad (4)$$

where f_{TI} is the Helmholtz free energy difference and f_{PV} is the PV contribution. Please refer to End Matter for detailed derivations in Eqs. (B1)–(B6). The accuracy of the CATI scheme is tested to be independent of the specific EAM potential (see Supplemental Material Note 5 [33]), as long as the reference potential can be smoothly connected to the *ab initio* state without phase transitions. A large amount of AIMD simulations were performed to compute the equilibrium volumes for liquid, superionic hcp, and bcc solutions at 5500–6000 K (Supplemental Material Fig. S16 [33]), which provides the f_{PV} term in Eq. (4). To obtain f_{TI} , a series of TI simulations from the classical system to the *ab initio* system were performed for liquid, superionic hcp, and superionic bcc solutions at 5500 K, as shown in Fig. 4(a). The TI path from the \mathcal{C} to the \mathcal{A} system is smooth, significantly reducing numerical errors in TI and enabling accurate determination of the free energy difference. With Eq. (4), G_A can be calculated for liquid, superionic hcp, and bcc at different O compositions (Supplemental Material Fig. S17 [33]). We also perform the free energy perturbation to include contributions of $3s^23p^6$ electrons, which have been shown to be necessary for accurately calculating

the free energy of Fe under IC conditions [22,62] (Supplemental Material Fig. S18 [33]).

Figure 4(b) shows the relative *ab initio* Gibbs free energy for liquid and superionic phases at 5500 K and 323 GPa. The regular solution model with the RK expansion in Eq. (2) can also well describe these free energies, providing fitting errors of less than 0.5 meV/atom (see Supplemental Material Fig. S9 [33]). Figure 4(b) shows the *ab initio* free energy of the superionic bcc phase is higher than that of the superionic hcp when the O composition is small. This is consistent with the fact that pure Fe prefers the hcp phase under IC conditions [22,23]. As the O composition increases, the free energy of the superionic hcp quickly increases. When the O composition is higher than 3 at.%, the superionic bcc phase becomes more stable than the superionic hcp phase. This can be related to the enhancement of Fe cooperative motion due to superionic O (Fig. 1), which increases the entropy of the bcc phase (Supplemental Material Note 8 [33]). Thus, the O composition in $\text{Fe}_{1-x}\text{O}_x$ changes the relative stability between the superionic bcc and hcp phases.

The common tangent line between liquid and superionic phases suggests that the superionic solution can only coexist with the liquid solution at small O compositions. Based on the $G_A^{SI-\text{hcp}}(x)$ and $G_A^L(x)$ curves, the common tangent line reveals *ab initio* solidus and liquidus points at 5500 K are $x_A^{SI-\text{hcp}} = 0.43\%$ and $x_A^L = 13.9\%$, respectively. Superionic hcp is more stable than superionic bcc at such a small O composition. We employ Eq. (3) to extend the free energy data to other temperatures for all three phases (Supplemental Material Fig. S19 [33]). The superionic hcp solidus and liquidus curves are computed using the common tangent approach. These data provide the *ab initio* phase diagram of superionic hcp and liquid $\text{Fe}_{1-x}\text{O}_x$ at 323 GPa in Fig. 4(c), with uncertainties analyzed in Supplemental Material Note 6 [33]. The superionic solidus line shows small temperature dependences, while the liquidus line depends on the temperature more strongly. It results in a partition coefficient strongly dependent on temperatures.

Oxygen concentration at ICB—The phase diagram in Fig. 4(c) indicates that the equilibrium O compositions in the solid IC and liquid outer core are highly correlated with the temperature at ICB. It provides a stronger constraint on the core's composition and temperature than the one from the partition coefficient data alone. Based on the phase diagram, the densities of $\text{Fe}_{1-x}\text{O}_x$ superionic and liquid solutions can be computed under the equilibrium conditions at different temperatures, as shown in Fig. 4(d). In previous work, substitutional O was introduced to account for the large density difference between the liquid and solid cores, i.e., the “density jump,” resulting in estimated O concentrations of 0.2 ± 0.1 at.% in the substitutional solid and 8.0 ± 2.5 at.% in the liquid solutions [63]. To assess the effect of superionic O, we follow the assumption in [63] by matching the density jump in PREM [64] using only O, but

based on the calculated equilibrium concentrations and densities of superionic hcp and liquid $\text{Fe}_{1-x}\text{O}_x$ solutions. It simultaneously constrains the O concentrations to 0.432 ± 0.003 at.% (0.124 ± 0.001 wt.%) in the superionic solid and 9.82 ± 1.45 at.% (3.02 ± 0.42 wt.%) in the liquid, along with a temperature of 5770 ± 86 K at the ICB. Therefore, compared to the previous substitutional solid solution, the superionic phase doubles O's solubility in hcp Fe under IC conditions. This extends the previously estimated range of O's concentration in the IC ($0 - 0.1$ wt.%), which are based on constraints from cosmochemistry, geochemistry, and mineral physics [24]. Our results add a missing piece by revealing the influence of the superionic state on these estimates. A different oxygen content in the IC can alter the energy release and thermal evolution of the core, potentially influencing core growth dynamics and the efficiency of compositional convection in the outer core, both essential for sustaining the geodynamo.

Our kinetic and thermodynamic data clarify the effect of superionic O on both the hcp and bcc phases. Since the bcc phase becomes more stable at O concentrations above 3 at.%, which likely fall within the estimated O content of the liquid core [24,65], this suggests that IC crystallization may begin with superionic bcc $\text{Fe}_{1-x}\text{O}_x$, especially considering the bcc phase exhibits a much higher nucleation rate than hcp [66]. Moreover, recent studies have shown that elements such as Ni and Si can further stabilize the bcc phase [67–70]. Based on these findings and our free energy data, mutual interactions among Ni, Si, and other light elements are expected to further influence both superionic O concentration and the stable crystalline phase in the IC. Therefore, *ab initio* Gibbs free energy calculations and phase diagrams of multicomponent Fe alloys—including the superionic state and various crystalline phases—are essential, and the present Letter provides a solid framework for such investigations.

In summary, we demonstrate that O can enter a superionic state in both hcp and bcc Fe under Earth's IC conditions. In particular, the superionic O enhances the cooperative diffusion of Fe atoms in the bcc lattice, increasing the entropy of the bcc phase and influencing the phase competition between hcp and bcc Fe. To accurately capture the thermodynamics of these complex phases, we develop an effective approach that combines classical coexistence simulations with *ab initio* free energy calculations to construct phase diagrams for nonstoichiometric superionic states. Applied to the $\text{Fe}_{1-x}\text{O}_x$ under IC conditions, our method quantitatively determines the Gibbs free energies of superionic bcc, superionic hcp, and liquid phases. The combination between the phase diagram and the density jump data simultaneously constrains the O composition and temperature at the ICB. Our results show that the presence of the superionic state nearly doubles the O content in hcp Fe compared to previous solid solution models. Moreover, superionic O emerges as an additional

stabilizing factor that lowers the free energy of bcc Fe at elevated O concentrations. The resulting Gibbs free energy data and superionic-liquid phase diagram provide new constraints on the composition and temperature of the IC, underscoring the critical role of superionicity in shaping Earth's core structure and evolution. The framework developed here establishes a foundation for investigating superionic–liquid equilibria in multicomponent Fe alloys under planetary interior conditions.

Acknowledgments—Work at Xiamen University was supported by the National Natural Science Foundation of China (Grants No. T2422016, No. 42550120, No. 42374108, and No. 12374015). The work at Columbia University was supported by the Gordon and Betty Moore Foundation Award No. GBMF12801 (doi.org/10.37807/GBMF12801). Shaorong Fang and Tianfu Wu from the Information and Network Center of Xiamen University are acknowledged for their help with Graphics Processing Unit computing. Some *ab initio* simulations were performed on Bridges-2 system at PSC, the Anvil system at Purdue University, the Expanse system at SDSC, and the Delta system at NCSA through allocation No. DMR180081 from the Advanced Cyberinfrastructure Coordination Ecosystem: Services & Support (ACCESS) program, which is supported by NSF Grants No. 2138259, No. 2138286, No. 2138307, No. 2137603, and No. 2138296. The supercomputing time were also supported by the Opening Project of the Joint Laboratory for Planetary Science and Supercomputing, Research Center for Planetary Science, and the National Supercomputing Center in Chengdu (Grants No. CSYYGS-QT-2024-15).

- [1] S. Hull, Superionics: Crystal structures and conduction processes, *Rep. Prog. Phys.* **67**, 1233 (2004).
- [2] Y. Li *et al.*, A lithium superionic conductor for millimeter-thick battery electrode, *Science* **381**, 50 (2023).
- [3] P. Demontis, R. LeSar, and M. L. Klein, New high-pressure phases of ice, *Phys. Rev. Lett.* **60**, 2284 (1988).
- [4] M. Millot, F. Coppari, J. R. Rygg, A. Correa Barrios, S. Hamel, D. C. Swift, and J. H. Eggert, Nanosecond x-ray diffraction of shock-compressed superionic water ice, *Nature (London)* **569**, 251 (2019).
- [5] J.-A. Hernandez and R. Caracas, Superionic-superionic phase transitions in body-centered cubic H₂O ice, *Phys. Rev. Lett.* **117**, 135503 (2016).
- [6] J.-A. Queyroux *et al.*, Melting curve and isostructural solid transition in superionic ice, *Phys. Rev. Lett.* **125**, 195501 (2020).
- [7] G. Weck, J.-A. Queyroux, S. Ninet, F. Datchi, M. Mezouar, and P. Loubeyre, Evidence and stability field of fcc superionic water ice using static compression, *Phys. Rev. Lett.* **128**, 165701 (2022).
- [8] M. Hou *et al.*, Superionic iron oxide–hydroxide in Earth's deep mantle, *Nat. Geosci.* **14**, 174 (2021).
- [9] C. Luo, Y. Sun, and R. M. Wentzcovitch, Probing the state of hydrogen in δ -AlOOH at mantle conditions with machine learning potential, *Phys. Rev. Res.* **6**, 013292 (2024).
- [10] Z. Wang, Y. He, H. Mao, and D. Y. Kim, Superionicity of oxygen-deficient davemaoite and its impact on the deep-Earth oxidation cycle, *Sci. Adv.* **11**, eadu8401 (2025).
- [11] C. Cavazzoni, G. L. Chiarotti, S. Scandolo, E. Tosatti, M. Bernasconi, and M. Parrinello, Superionic and metallic states of water and ammonia at giant planet conditions, *Science* **283**, 44 (1999).
- [12] R. Redmer, T. R. Mattsson, N. Nettelmann, and M. French, The phase diagram of water and the magnetic fields of Uranus and Neptune, *Icarus* **211**, 798 (2011).
- [13] J. Sun, B. K. Clark, S. Torquato, and R. Car, The phase diagram of high-pressure superionic ice, *Nat. Commun.* **6**, 8156 (2015).
- [14] B. Cheng, M. Bethkenhagen, C. J. Pickard, and S. Hamel, Phase behaviours of superionic water at planetary conditions, *Nat. Phys.* **17**, 1228 (2021).
- [15] H. Gao, C. Liu, J. Shi, S. Pan, T. Huang, X. Lu, H.-T. Wang, D. Xing, and J. Sun, Superionic silica-water and silicahydrogen compounds in the deep interiors of Uranus and Neptune, *Phys. Rev. Lett.* **128**, 035702 (2022).
- [16] J.-A. Hernandez, M. Bethkenhagen, S. Ninet, M. French, A. Benuzzi-Mounaix, F. Datchi, M. Guaraguaglini, F. Lefevre, F. Occelli, and R. Redmer, Melting curve of superionic ammonia at planetary interior conditions, *Nat. Phys.* **19**, 1280 (2023).
- [17] C. Liu, H. Gao, Y. Wang, R. J. Needs, C. J. Pickard, J. Sun, H.-T. Wang, and D. Xing, Multiple superionic states in helium–water compounds, *Nat. Phys.* **15**, 1065 (2019).
- [18] Y. He, S. Sun, D. Y. Kim, B. G. Jang, H. Li, and H. Mao, Superionic iron alloys and their seismic velocities in Earth's inner core, *Nature (London)* **602**, 258 (2022).
- [19] S. Sun, Y. He, J. Yang, Y. Lin, J. Li, D. Y. Kim, H. Li, and H. Mao, Superionic effect and anisotropic texture in Earth's inner core driven by geomagnetic field, *Nat. Commun.* **14**, 1656 (2023).
- [20] K. Hirose, S. Labrosse, and J. Hernlund, Composition and state of the core, *Annu. Rev. Earth Planet Sci.* **41**, 657 (2013).
- [21] A. B. Belonoshko, T. Lukinov, J. Fu, J. Zhao, S. Davis, and S. I. Simak, Stabilization of body-centred cubic iron under inner-core conditions, *Nat. Geosci.* **10**, 312 (2017).
- [22] Y. Sun, M. I. Mendelev, F. Zhang, X. Liu, B. Da, C.-Z. Wang, R. M. Wentzcovitch, and K.-M. Ho, Ab initio melting temperatures of bcc and hcp iron under the Earth's inner core condition, *Geophys. Res. Lett.* **50**, e2022GL102447 (2023).
- [23] F. González-Cataldo and B. Militzer, Ab initio determination of iron melting at terapascal pressures and super-Earths core crystallization, *Phys. Rev. Res.* **5**, 033194 (2023).
- [24] K. Hirose, B. Wood, and L. Vočadlo, Light elements in the Earth's core, *Nat. Rev. Earth Environ.* **2**, 645 (2021).
- [25] M. Pozzo, C. Davies, D. Gubbins, and D. Alfè, FeO content of Earth's liquid core, *Phys. Rev. X* **9**, 041018 (2019).

- [26] D. Alfe, M. Gillan, and G. Price, Ab initio chemical potentials of solid and liquid solutions and the chemistry of the Earth's core, *J. Chem. Phys.* **116**, 7127 (2002).
- [27] J. P. Poirier, Light elements in the Earth's outer core: A critical review, *Phys. Earth Planet. Inter.* **85**, 319 (1994).
- [28] J. Klarbring and S. I. Simak, Phase stability of dynamically disordered solids from first principles, *Phys. Rev. Lett.* **121**, 225702 (2018).
- [29] H. F. Wilson, M. L. Wong, and B. Militzer, Superionic to superionic phase change in water: Consequences for the interiors of uranus and neptune, *Phys. Rev. Lett.* **110**, 151102 (2013).
- [30] V. Fidalgo Cândido, F. Matusalem, and M. de Koning, Melting conditions and entropies of superionic water ice: Free-energy calculations based on hybrid solid/liquid reference systems, *J. Chem. Phys.* **158**, 064502 (2023).
- [31] F. Wu, S. Wu, C.-Z. Wang, K.-M. Ho, R. M. Wentzcovitch, and Y. Sun, Melting temperature of iron under the Earth's inner core condition from deep machine learning, *Geosci. Front.* **15**, 101925 (2024).
- [32] A. Reinhardt and B. Cheng, Quantum-mechanical exploration of the phase diagram of water, *Nat. Commun.* **12**, 588 (2021).
- [33] See Supplemental Material at <http://link.aps.org/supplemental/10.1103/37nh-5ws8> for details of the EAM potential development, the uncertainties in the phase diagram, and the additional free energy data analysis, which includes additional Refs. [34–57].
- [34] A. B. Belonoshko, T. Lukinov, J. Fu, J. Zhao, S. Davis, and S. I. Simak, Stabilization of body-centred cubic iron under inner-core conditions, *Nat. Geosci.* **10**, 312 (2017).
- [35] M. Ghosh, S. Zhang, L. Hu, and S. Hu, Cooperative diffusion in body-centered cubic iron in Earth and super-Earths' inner core conditions, *J. Phys. Condens. Matter* **35**, 154002 (2023).
- [36] Y.-Y. Ye, Y. Chen, K.-M. Ho, B. N. Harmon, and P.-A. Lindgrd, Phonon-phonon coupling and the stability of the high-temperature bcc phase of Zr, *Phys. Rev. Lett.* **58**, 1769 (1987).
- [37] R. M. Wentzcovitch and M. L. Cohen, Theoretical model for the hcp-bcc transition in Mg, *Phys. Rev. B* **37**, 5571 (1988).
- [38] C. J. Davies, M. Pozzo, and D. Alfè, Assessing the inner core nucleation paradox with atomic-scale simulations, *Earth Planet. Sci. Lett.* **507**, 1 (2019).
- [39] Y. He, S. Sun, D. Y. Kim, B. G. Jang, H. Li, and H. Mao, Superionic iron alloys and their seismic velocities in Earth's inner core, *Nature (London)* **602**, 258 (2022).
- [40] R. Paula Leite, R. Freitas, R. Azevedo, and M. de Koning, The Uhlenbeck-Ford model: Exact virial coefficients and application as a reference system in fluid-phase free-energy calculations, *J. Chem. Phys.* **145**, 194101 (2016).
- [41] R. Paula Leite, P. A. Santos-Florez, and M. de Koning, Uhlenbeck-Ford model: Phase diagram and corresponding-states analysis, *Phys. Rev. E* **96**, 032115 (2017).
- [42] S. Cajahuaranga and A. Antonelli, Nonequilibrium free energy methods applied to magnetic systems: The degenerate Ising model, *J. Stat. Phys.* **175**, 1006 (2019).
- [43] S. Menon, Y. Lysogorskiy, J. Rogal, and R. Drautz, Automated free-energy calculation from atomistic simulations, *Phys. Rev. Mater.* **5**, 103801 (2021).
- [44] R. Paula Leite and M. de Koning, Nonequilibrium free-energy calculations of fluids using LAMMPS, *Comput. Mater. Sci.* **159**, 316 (2019).
- [45] O. Redlich and A. Kister, Algebraic representation of thermodynamic properties and the classification of solutions, *Ind. Eng. Chem.* **40**, 345 (1948).
- [46] Z.-K. Liu, Computational thermodynamics and its applications, *Acta Mater.* **200**, 745 (2020).
- [47] C. Vega, E. Sanz, J. Abascal, and E. Noya, Determination of phase diagrams via computer simulation: Methodology and applications to water, electrolytes and proteins, *J. Phys. Condens. Matter* **20**, 153101 (2008).
- [48] J. P. Perdew, K. Burke, and M. Ernzerhof, Generalized gradient approximation made simple, *Phys. Rev. Lett.* **77**, 3865 (1996).
- [49] J. P. Perdew, A. Ruzsinszky, G. I. Csonka, O. A. Vydrov, G. E. Scuseria, L. A. Constantin, X. Zhou, and K. Burke, Restoring the density-gradient expansion for exchange in solids and surfaces, *Phys. Rev. Lett.* **100**, 136406 (2008).
- [50] J. Sun, A. Ruzsinszky, and J. P. Perdew, Strongly constrained and appropriately normed semilocal density functional, *Phys. Rev. Lett.* **115**, 036402 (2015).
- [51] J. Zhuang, H. Wang, Q. Zhang, and R. M. Wentzcovitch, Thermodynamic properties of ϵ -Fe with thermal electronic excitation effects on vibrational spectra, *Phys. Rev. B* **103**, 144102 (2021).
- [52] A. Dewaele, P. Loubeyre, F. Occelli, M. Mezouar, P. I. Dorogokupets, and M. Torrent, Quasihydrostatic equation of state of iron above 2 Mbar, *Phys. Rev. Lett.* **97**, 215504 (2006).
- [53] H. Mao, Y. Wu, L. Chen, J. Shu, and A. P. Jephcoat, Static compression of iron to 300 GPa and $\text{Fe}_{0.8}\text{Ni}_{0.2}$ alloy to 260 GPa: Implications for composition of the core, *J. Geophys. Res. Solid Earth* **95**, 21737 (1990).
- [54] L. S. Dubrovinsky, S. K. Saxena, F. Tutti, S. Rekhi, and T. LeBehan, In situ x-ray study of thermal expansion and phase transition of iron at multimegabar pressure, *Phys. Rev. Lett.* **84**, 1720 (2000).
- [55] T. Sakai, S. Takahashi, N. Nishitani, I. Mashino, E. Ohtani, and N. Hirao, Equation of state of pure iron and $\text{Fe}_{0.9}\text{Ni}_{0.1}$ alloy up to 3 Mbar, *Phys. Earth Planet. Inter.* **228**, 114 (2014).
- [56] Y. Fei, C. Murphy, Y. Shibasaki, A. Shahar, and H. Huang, Thermal equation of state of hcp-iron: Constraint on the density deficit of Earth's solid inner core, *Geophys. Res. Lett.* **43**, 6837 (2016).
- [57] The ELK code, <http://elk.sourceforge.net>.
- [58] M. Ghosh, S. Zhang, L. Hu, and S. Hu, Cooperative diffusion in body-centered cubic iron in Earth and super-Earths' inner core conditions, *J. Phys. Condens. Matter* **35**, 154002 (2023).
- [59] M. S. Daw and M. I. Baskes, Embedded-atom method: Derivation and application to impurities, surfaces, and other defects in metals, *Phys. Rev. B* **29**, 6443 (1984).
- [60] O. Redlich and A. Kister, Algebraic representation of thermodynamic properties and the classification of solutions, *Ind. Eng. Chem.* **40**, 345 (1948).
- [61] D. Alfe, M. Gillan, and G. Price, The melting curve of iron at the pressures of the Earth's core from ab initio calculations, *Nature (London)* **401**, 462 (1999).

- [62] T. Sun, J. P. Brodholt, Y. Li, and L. Vočadlo, Melting properties from ab initio free energy calculations: Iron at the Earth's inner-core boundary, *Phys. Rev. B* **98**, 224301 (2018).
- [63] D. Alfè, M. J. Gillan, and G. D. Price, Composition and temperature of the Earth's core constrained by combining ab initio calculations and seismic data, *Earth Planet. Sci. Lett.* **195**, 91 (2002).
- [64] A. M. Dziewonski and D. L. Anderson, Preliminary reference Earth model, *Phys. Earth Planet. Inter.* **25**, 297 (1981).
- [65] J. Badro, A. S. Côté, and J. P. Brodholt, A seismologically consistent compositional model of Earth's core, *Proc. Natl. Acad. Sci. U.S.A.* **111**, 7542 (2014).
- [66] Y. Sun, F. Zhang, M. I. Mendelev, R. M. Wentzcovitch, and K.-M. Ho, Two-step nucleation of the Earth's inner core, *Proc. Natl. Acad. Sci. U.S.A.* **119**, e2113059119 (2022).
- [67] Y. Sun, M. I. Mendelev, F. Zhang, X. Liu, B. Da, C. Z. Wang, R. M. Wentzcovitch, and K. M. Ho, Unveiling the effect of Ni on the formation and structure of Earth's inner core, *Proc. Natl. Acad. Sci. U.S.A.* **121**, e2316477121 (2024).
- [68] D. Ikuta, E. Ohtani, and N. Hirao, Two-phase mixture of iron-nickel-silicon alloys in the Earth's inner core, *Commun. Earth Environ.* **2**, 225 (2021).
- [69] Z. Li and S. Scandolo, Short-range order stabilizes a cubic iron alloy in Earth's inner core, *Nat. Comm.* **16**, 7574 (2025).
- [70] L. Wei, Z. Wu, K.-M. Ho, R. M. Wentzcovitch, and Y. Sun, The Fe-Ni phase diagram and the Earth's inner core structure, *Sci. Adv.* **11**, eadu1998 (2025).
- [71] D. R. Gaskell and D. E. Laughlin, *Introduction to the Thermodynamics of Materials* (CRC Press, New York, 2017).
- [72] A. P. Thompson, H. M. Aktulga, R. Berger, D. S. Bolintineanu, W. M. Brown, P. S. Crozier, P. J. In't Veld, A. Kohlmeyer, S. G. Moore, and T. D. Nguyen, LAMMPS—a flexible simulation tool for particle-based materials modeling at the atomic, meso, and continuum scales, *Comput. Phys. Commun.* **271**, 108171 (2022).
- [73] R. M. Wentzcovitch, Invariant molecular-dynamics approach to structural phase transitions, *Phys. Rev. B* **44**, 2358 (1991).
- [74] C. J. Davies, M. Pozzo, and D. Alfè, Assessing the inner core nucleation paradox with atomic-scale simulations, *Earth Planet. Sci. Lett.* **507**, 1 (2019).
- [75] J. Hafner, Ab-initio simulations of materials using VASP: Density-functional theory and beyond, *J. Comput. Chem.* **29**, 2044 (2008).
- [76] G. Kresse and J. Furthmüller, Efficient iterative schemes for ab initio total-energy calculations using a plane-wave basis set, *Phys. Rev. B* **54**, 11169 (1996).
- [77] P. E. Blöchl, Projector augmented-wave method, *Phys. Rev. B* **50**, 17953 (1994).
- [78] J. P. Perdew, K. Burke, and M. Ernzerhof, Generalized gradient approximation made simple, *Phys. Rev. Lett.* **77**, 3865 (1996).
- [79] N. D. Mermin, Thermal properties of the inhomogeneous electron gas, *Phys. Rev.* **137**, A1441 (1965).
- [80] R. M. Wentzcovitch, J. L. Martins, and P. B. Allen, Energy versus free-energy conservation in first-principles molecular dynamics, *Phys. Rev. B* **45**, 11372 (1992).

End Matter

Free energy relation in the superionic-liquid equilibrium—Let us consider the thermodynamic equilibrium in a superionic-liquid coexistence system. We use $G^L(x^L, T, P)$ and $G^{SI}(x^{SI}, T, P)$ to represent the absolute Gibbs free energy of the liquid and superionic phases, respectively. x^L and x^{SI} represent the O content in the liquid and superionic $\text{Fe}_{1-x}\text{O}_x$, respectively. The Gibbs free energy of the liquid and superionic solutions at temperature T and pressure P can be expressed as

$$\begin{aligned} G^L(x^L, T, P) &= x^L \bar{G}_o^L(x^L, T, P) \\ &\quad + (1 - x^L) \bar{G}_{Fe}^L(x^L, T, P), \end{aligned} \quad (\text{A1a})$$

$$\begin{aligned} G^{SI}(x^{SI}, T, P) &= x^{SI} \bar{G}_o^{SI}(x^{SI}, T, P) \\ &\quad + (1 - x^{SI}) \bar{G}_{Fe}^{SI}(x^{SI}, T, P), \end{aligned} \quad (\text{A1b})$$

where $\bar{G}_o^L(x^L, T, P)$ and $\bar{G}_{Fe}^L(x^L, T, P)$ are the partial molar Gibbs free energy of oxygen and iron in the liquid solutions, respectively. $\bar{G}_o^{SI}(x^{SI}, T, P)$ and $\bar{G}_{Fe}^{SI}(x^{SI}, T, P)$ are the partial molar Gibbs free energy of oxygen and iron in the superionic solutions, respectively. Taking the derivative of both sides of Eqs. (A1a) and

(A1b) with respect to x^L and x^{SI} and the Gibbs-Duhem relation, we get

$$\frac{\partial G^L(x, T, P)}{\partial x} \Big|_{x=x^L} = \bar{G}_o^L(x^L, T, P) - \bar{G}_{Fe}^L(x^L, T, P), \quad (\text{A2a})$$

$$\frac{\partial G^{SI}(x, T, P)}{\partial x} \Big|_{x=x^{SI}} = \bar{G}_o^{SI}(x^{SI}, T, P) - \bar{G}_{Fe}^{SI}(x^{SI}, T, P). \quad (\text{A2b})$$

By combining Eqs. (A1) and (A2) and eliminating $\bar{G}_{Fe}^L(x^L, T, P)$ and $\bar{G}_{Fe}^{SI}(x^{SI}, T, P)$, we can obtain the partial molar Gibbs free energy of oxygen in both liquid and superionic $\text{Fe}_{1-x}\text{O}_x$ as follows:

$$\begin{aligned} \bar{G}_o^L(x^L, T, P) &= G^L(x^L, T, P) \\ &\quad + (1 - x^L) \frac{\partial G^L(x, T, P)}{\partial x} \Big|_{x=x^L}, \end{aligned} \quad (\text{A3a})$$

$$\begin{aligned} \bar{G}_o^{SI}(x^{SI}, T, P) &= G^{SI}(x^{SI}, T, P) \\ &\quad + (1 - x^{SI}) \frac{\partial G^{SI}(x, T, P)}{\partial x} \Big|_{x=x^{SI}}. \end{aligned} \quad (\text{A3b})$$

By combining Eqs. (A2) and (A3), the partial molar Gibbs free energy of iron in liquid and superionic solutions are as follows:

$$\bar{G}_{Fe}^L(x^L, T, P) = G^L(x^L, T, P) - x^L \frac{\partial G^L(x, T, P)}{\partial x} \Big|_{x=x^L}, \quad (\text{A4a})$$

$$\bar{G}_{Fe}^{SI}(x^{SI}, T, P) = G^{SI}(x^{SI}, T, P) - x^{SI} \frac{\partial G^{SI}(x, T, P)}{\partial x} \Big|_{x=x^{SI}}. \quad (\text{A4b})$$

When the liquid and superionic solutions reach equilibrium at the temperature T_0 and pressure P_0 , the partial molar Gibbs free energy of both iron and oxygen in both phases are equal [71]. Therefore, they satisfy

$$\bar{G}_o^L(x_0^L, T_0, P_0) = \bar{G}_o^{SI}(x_0^{SI}, T_0, P_0), \quad (\text{A5a})$$

$$\bar{G}_{Fe}^L(x_0^L, T_0, P_0) = \bar{G}_{Fe}^{SI}(x_0^{SI}, T_0, P_0), \quad (\text{A5b})$$

where x_0^L and x_0^{SI} are the oxygen contents in liquid and superionic solutions when the coexistence system reaches equilibrium at the fixed temperature T_0 and pressure P_0 . So that we have,

$$\frac{\partial G^L(x, T_0, P_0)}{\partial x} \Big|_{x=x_0^L} = \frac{\partial G^{SI}(x, T_0, P_0)}{\partial x} \Big|_{x=x_0^{SI}}, \quad (\text{A6a})$$

$$\begin{aligned} G^L(x_0^L, T_0, P_0) - x_0^L \frac{\partial G^L(x, T_0, P_0)}{\partial x} \Big|_{x=x_0^L} \\ = G^{SI}(x_0^{SI}, T_0, P_0) - x_0^{SI} \frac{\partial G^{SI}(x, T_0, P_0)}{\partial x} \Big|_{x=x_0^{SI}}. \end{aligned} \quad (\text{A6b})$$

By Eq. (A6), the absolute Gibbs free energy of the superionic with an oxygen molar fraction x_0^{SI} is as follows:

$$G^{SI}(x_0^{SI}, T_0, P_0) = G^L(x_0^L, T_0, P_0) - (x_0^L - x_0^{SI}) \frac{\partial G^L(x)}{\partial x} \Big|_{x=x_0^L}. \quad (\text{A7})$$

Equation (A7) indicates that if the oxygen concentrations in the superionic-liquid equilibrium and the liquid free energy are known, the Gibbs free energy of the superionic phase can be directly calculated. It is straightforward to obtain these quantities using large-scale MD simulations with interatomic potentials.

Thermodynamic integration from classical to ab initio systems—When the Gibbs free energy $G_C(x, T_0, P_0)$ of the classical system is available, the TI scheme can be

performed to obtain the Gibbs free energy $G_A(x, T_0, P_0)$ at *ab initio* level [22,61]. We note the volumes of \mathcal{A} and \mathcal{C} systems as V_A and V_C at the pressure P_0 . The Gibbs free energy can be written as follows,

$$\begin{aligned} & G_A(x, T_0, P_0) - G_C(x, T_0, P_0) \\ &= F_A(x, T_0, V_A) + P_0 V_A(x, T_0, P_0) \\ &\quad - F_C(x, T_0, V_C) - P_0 V_C(x, T_0, P_0), \end{aligned} \quad (\text{B1})$$

where F_A and F_C are the Helmholtz free energy of \mathcal{A} and \mathcal{C} systems, respectively. Here, $F_A(x, T_0, V_A) - F_C(x, T_0, V_C)$ term can be written as

$$\begin{aligned} & F_A(x, T_0, V_A) - F_C(x, T_0, V_C) \\ &= (F_A(x, T_0, V_A) - F_C(x, T_0, V_A)) \\ &\quad + (F_C(x, T_0, V_A) - F_C(x, T_0, V_C)). \end{aligned} \quad (\text{B2})$$

Because $P = -(\partial F / \partial V)_T$, we can write

$$F_C(x, T_0, V_A) - F_C(x, T_0, V_C) = - \int_{V_C}^{V_A} P_C(x, V, T_0) dV, \quad (\text{B3})$$

We define f_{PV} as

$$f_{PV}(x, T_0, P_0) = P_0 V_A - P_0 V_C - \int_{V_C}^{V_A} P_C(x, V, T_0) dV, \quad (\text{B4})$$

where $P_C(x, V, T_0)$ is the equation of states of the solution for system \mathcal{C} . The f_{PV} term requires the equilibrium volumes of the solution for systems \mathcal{A} and \mathcal{C} , respectively. We also define $F_A(x, T_0, V_A) - F_C(x, T_0, V_A)$ as the f_{TI} term, which can be calculated by TI using the classical system as the reference state [22], i.e.,

$$\begin{aligned} f_{TI}(x, T_0, P_0) &= F_A(x, T_0, V_A) - F_C(x, T_0, V_A) \\ &= \int_0^1 \langle U_A(x, T_0, V_A) \\ &\quad - U_C(x, T_0, V_A) \rangle_{\lambda, NVT} d\lambda, \end{aligned} \quad (\text{B5})$$

where U_A and U_C are the internal energy of solutions for systems \mathcal{A} and \mathcal{C} , respectively. $\langle \cdot \rangle_{\lambda, NVT}$ is the ensemble average of internal energy over configurations sampled in the canonical ensemble with the force field $U = (1 - \lambda)U_C + \lambda U_A$. The subscript *NVT* indicates the constant conditions of volume (V_A) and temperature (T_0) in the MD simulations of TI.

Combining Eqs. (B1)–(B5), the *ab initio* Gibbs free energy for liquid and superionic solutions can be obtained as

$$\begin{aligned} G_A(x, T_0, P_0) &= G_C(x, T_0, P_0) + f_{PV}(x, T_0, P_0) \\ &\quad + f_{TI}(x, T_0, P_0). \end{aligned} \quad (\text{B6})$$

With Eq. (B6), G_A can be calculated for liquid, superionic hcp, and bcc at any oxygen composition, temperature, and pressure.

Simulation details—Classical MD simulations were performed using the large-scale atomic and molecular massively parallel simulator (LAMMPS) code [72]. The embedded-atom method (EAM) potential was developed to simulate superionic Fe-O systems under Earth's core conditions. The time step in the classical MD simulation was 1.0 fs. The Nosé-Hoover thermostat and barostat obeying modular invariance [73] were applied with the damping time $\tau = 0.1$ ps; 323 GPa was chosen as the target pressure to maintain consistency with previous free energy calculations [22,67,70,74].

Ab initio molecular dynamics (AIMD) simulations were performed using the Vienna *ab initio* simulation package (VASP) [75,76]. The projected augmented wave (PAW) method [77] was used to describe the electron-ion interaction. The generalized gradient approximation (GGA) in the Perdew-Burke-Ernzerhof (PBE) form [78] was employed for the exchange-correlation energy functional. Tests with other exchange-correlation functionals (PBEsol and SCAN) suggest that the PBE functional provides the best description of Fe's equation of state (EOS) at high

pressures, compared to experimental data (Supplemental Material Note 7 [33]). The electronic entropy was included using the Mermin functional [79,80] and the electronic temperature in the Mermin functional was the same as the ionic temperature. Supercells with 250, 288–293, and 250–254 atoms were used for liquid, superionic hcp and superionic bcc phases, respectively. The size of the simulation cell is found to have a negligible effect on the free energy calculation of bcc Fe (Supplemental Material Fig. S10 [33]). The time step in AIMD and TI was 1 fs. PAW potential with $3d^74s^1$ valence electrons (noted as PAW8) was used for Fe in the AIMD and TI. PAW potential with $3s^23p^63d^74s^1$ valence electrons (noted as PAW16) was used in the FEP. PAW potential with $2s^22p^4$ valence electrons was used for O. The plane-wave cutoff was 400 eV for PAW8-Fe and 750 eV for PAW16-Fe. The Γ point was used in the AIMD. A dense Monkhorst-Pack k -point mesh of $2 \times 2 \times 2$ was adopted for superionic and liquid phases to achieve a high DFT accuracy in the FEP calculations. The PAW16 potential produces an EOS consistent with all-electron calculations for both hcp and bcc Fe. (Supplemental Material Note 7 [33]). For a target pressure, the lattice parameters of bcc, hcp, and liquid phases were adjusted for each temperature and composition to ensure the pressure fluctuated around the target value by less than 0.5 GPa within 5 ps of simulations. The enthalpy data were collected from AIMD lasting more than 10 ps.

Supplementary Materials

***Ab initio* superionic-liquid phase diagram of Fe_{1-x}O_x under Earth's inner core conditions**

Zepeng Wu¹, Chen Gao¹, Feng Zhang², Shunqing Wu¹,
Kai-Ming Ho², Renata M. Wentzcovitch³⁻⁶, Yang Sun¹

¹*Department of Physics, Xiamen University, Xiamen 361005, China*

²*Department of Physics, Iowa State University, Ames, IA 50011, USA*

³*Department of Applied Physics and Applied Mathematics, Columbia University, New York, NY 10027, USA*

⁴*Department of Earth and Environmental Sciences, Columbia University, New York, NY 10027, USA*

⁵*Lamont–Doherty Earth Observatory, Columbia University, Palisades, NY 10964, USA*

⁶*Data Science Institute, Columbia University, New York, NY 10027, USA*

Contents

Notes 1-8

Figures S1-S19

Table S1

References

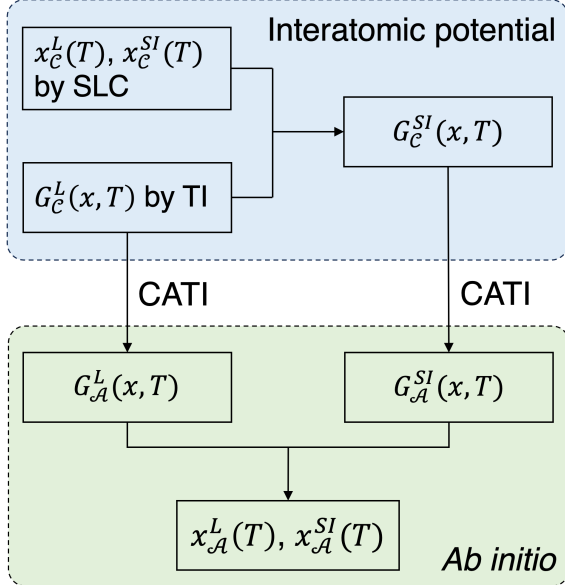


Fig. S1 Schematic workflow. SLC: solid-liquid coexistence simulation. TI: conventional thermodynamic integration from the liquid model. CATI refers to classical-to-*ab initio* thermodynamic integration. x_C^L , x_C^{SI} : classical liquidus and superionic solidus; G_C^L , G_C^{SI} : Gibbs free energy of liquid and superionic solutions at the classical level of the interatomic potential. x_A^L , x_A^{SI} : *ab initio* liquidus and superionic solidus. G_A^L , G_A^{SI} : Gibbs free energy of liquid and superionic solutions at the *ab initio* level.

Supplementary Note 1 | The effect of interstitial oxygen on the instability of bcc Fe

It has been suggested that the cooperative diffusion of Fe atoms originates from the inherent instability of the bcc lattice [1]. This instability is evidenced by imaginary phonon modes in the bcc lattice of Fe at 0 K [2]. At high temperatures, these imaginary modes promote cooperative Fe diffusion, dynamically stabilizing the bcc lattice. To quantitatively analyze the enhanced Fe diffusion in the presence of superionic oxygen, we study how the interstitial oxygen affects the unstable phonon modes. Figure S2(a) shows the phonon spectrum of bcc Fe at 323 GPa, which exhibits an imaginary phonon mode at the N point responsible for the hcp–bcc martensitic transition [3,4]. The vibrational pattern of the imaginary phonon mode is shown in Fig. S2(b), corresponding to a collective displacement of atomic layers along the [110] direction. By displacing Fe atoms along these eigenmodes, we obtain a double-well potential energy surface, as shown in Fig. S2(e), confirming the structural instability associated with the imaginary mode. To examine the effect of oxygen, we place one and two oxygen atoms at interstitial sites in the bcc

lattice shown in Fig. S2(c) and (d), and evaluate the resulting changes in the potential energy surface. We find that the introduction of oxygen deepens the potential well near the instability point, indicating that oxygen atoms enhance the tendency of Fe atoms to deviate from their ideal lattice positions. This mechanism suggests that superionic oxygen at high temperatures can further amplify the deviation of Fe atoms from lattice sites and promote cooperative diffusion within the bcc lattice.

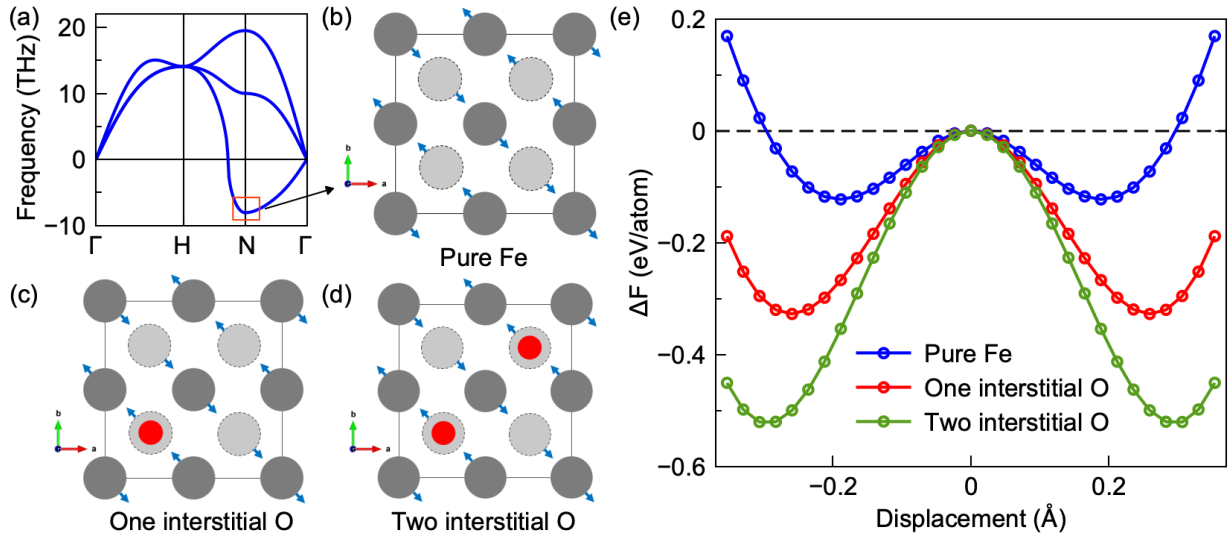


Fig. S2 (a) Phonon spectrum of bcc Fe at 323 GPa and $T_{\text{elec}}=5500$ K. (b) Imaginary phonon modes at N point in perfect bcc Fe. Black solid circles represent Fe atoms with fractional coordinate $z=0$, while dashed-border circles represent Fe atoms with $z=0.5$. Blue arrows indicate the eigenvector of the imaginary mode. (c) bcc Fe with one oxygen atom (red) at the interstitial site $(0.25, 0.25, 0)$, and (d) with two oxygen atoms at interstitial sites $(0.25, 0.25, 0)$ and $(0.75, 0.75, 0)$. (e) Potential energy surface along atomic displacement corresponding to the imaginary phonon mode.

Supplementary Note 2 | The Fe-O EAM potential

The embedded-atom method (EAM) potential of the Fe-O system under Earth's core conditions was previously developed [5] to study the nucleation of Earth's inner core. As shown in Fig. S3(a), when simulating the *hcp* supercell containing 384 Fe atoms and 24 interstitial O atoms, the structure becomes unstable with the EAM potential from Ref. [5]. However, the superionic state should be dynamically stable according to the *ab initio* molecular dynamics (AIMD) simulation of the same O composition under such conditions [6]. To stabilize the superionic state, we found it is critical to reduce the Fe-O interactions. The modified EAM potential can now simulate the

superionic phase, as shown in Fig. S3(b). The mean squared displacement of superionic hcp, superionic bcc, and liquid phases simulated by the modified EAM potential is similar to those from AIMD simulation as shown in Fig. S4.

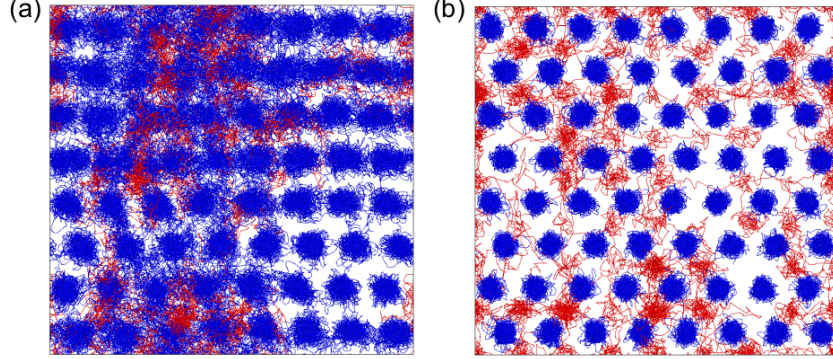


FIG. S3 Simulation of superionic phase with different EAM potentials. (a) The atomic trajectories of hcp $\text{Fe}_{384}\text{O}_{24}$ ($\text{FeO}_{0.0625}$) from MD simulation at 323 GPa, 5000 K with EAM potential developed by Davies et al. [5]. The blue (red) lines represent the atomic trajectories of iron (oxygen) atoms. (b) The atomic trajectories of hcp $\text{Fe}_{384}\text{O}_{24}$ from MD simulation with EAM potential developed in this work.

The analytic form of present EAM potential is shown below. The parameters are as shown in Table S1. The energy of the EAM potential is

$$E_{tot} = \sum_{i_{Fe}} E_{i_{Fe}} + \sum_{i_O} E_{i_O} + \sum_{i_{FeO}} E_{i_{FeO}}, \quad (S1)$$

where i_{Fe} runs over the Fe atoms, i_O over the O atoms and i_{FeO} over the whole Fe-O pairs.

The atomic energies are

$$E_{i_{Fe}} = \sum_{j_{Fe} \neq i_{Fe}} \epsilon_{Fe} \left(\frac{a_{Fe}}{r_{i_{Fe} j_{Fe}}} \right)^{n_{Fe}} - \epsilon_{Fe} C_{Fe} \sqrt{\rho_{i_{Fe}}}, \quad (S2)$$

$$E_{i_O} = \sum_{j_O \neq i_O} \epsilon_O \left(\frac{a_O}{r_{i_O j_O}} \right)^{n_O} - \epsilon_O C_O \sqrt{\rho_{i_O}}, \quad (S3)$$

$$E_{i_{FeO}} = \frac{1}{2} \sum_{i_{Fe} \neq j_O} \epsilon_{FeO} \left(\frac{a_{FeO}}{r_{i_{Fe} j_O}} \right)^{n_{FeO}}. \quad (S4)$$

The density terms are as follows

$$\rho_{i_{Fe}} = \sum_{j_{Fe} \neq i_{Fe}} \left(\frac{a_{Fe}}{r_{i_{Fe} j_{Fe}}} \right)^{m_{Fe}} + \sum_{j_O} \left(\frac{a_{FeO}}{r_{i_{Fe} j_O}} \right)^{m_{FeO}}, \quad (S5)$$

$$\rho_{i_O} = \sum_{j_O \neq i_O} \left(\frac{a_O}{r_{i_O j_O}} \right)^{m_O} + \sum_{j_{Fe}} \left(\frac{a_{FeO}}{r_{i_O j_{Fe}}} \right)^{m_{FeO}}. \quad (S6)$$

Table S1 Parameters for the EAM potential developed in this work.

	ϵ (eV)	a (Å)	n	m	C
Fe	0.1662	3.471	5.930	4.788	17.378
O	0.0885	2.602	9.170	7.483	16.400
Fe-O	0.1810	3.408	4.796	4.731	-

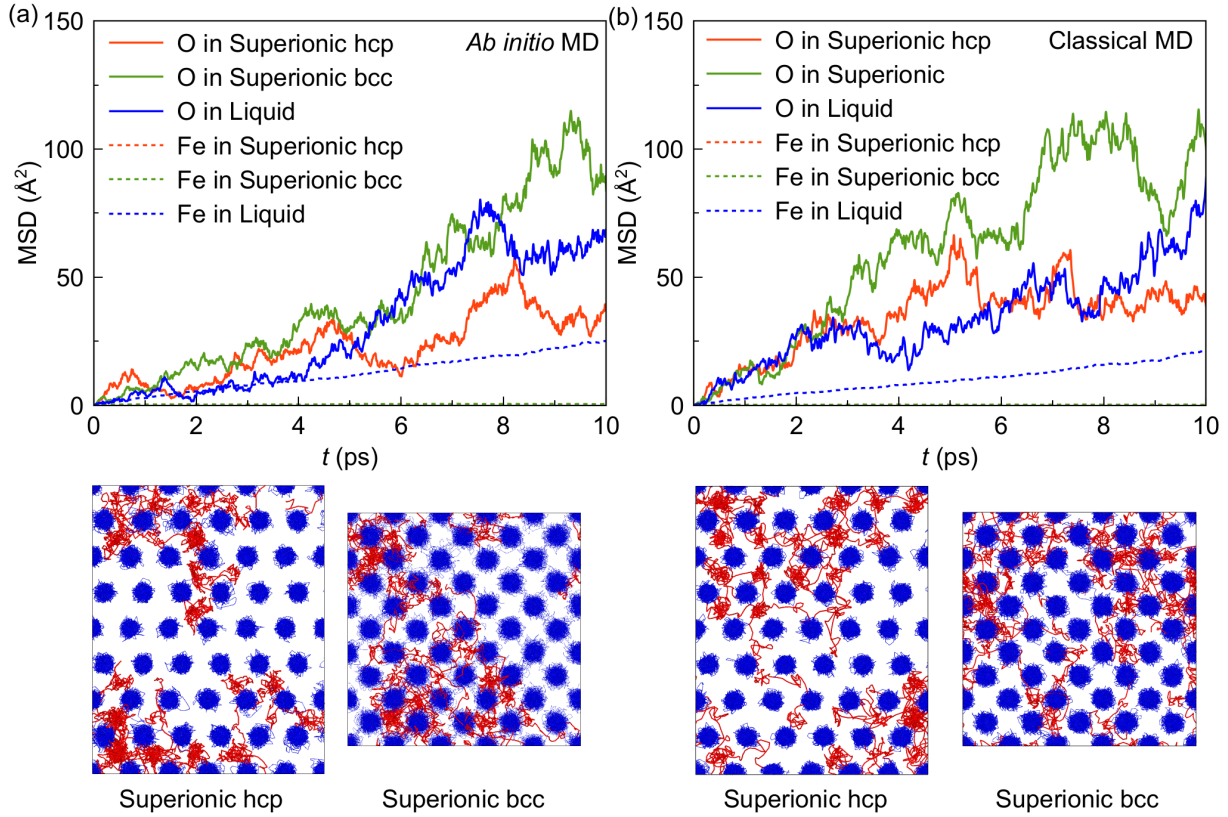


FIG. S4 Mean squared displacement (MSD) of iron and oxygen atoms in liquid, superionic hcp and superionic bcc $\text{Fe}_{0.99}\text{O}_{0.01}$ at 5500 K and 323 GPa from (a) AIMD and (b) classical MD simulations over 10 ps. The lower panels represent the atomic trajectories of two superionic phases. The red (blue) represents the oxygen (iron) atoms.

Supplementary Note 3 | Gibbs free energy calculation of liquid

With the interatomic potential, the composition-dependent Gibbs free energy for the liquid solution of any x can be readily computed as

$$G_{\mathcal{C}}^L(x, T_0, P_0) = P_0 V_{\mathcal{C}}^L(x, T_0, P_0) + F_{\mathcal{C}}^L(x, T_0, V_{\mathcal{C}}^L), \quad (\text{S7})$$

where $V_{\mathcal{C}}^L(x, T_0, P_0)$ is the volume of the liquid solution at (x, P_0, T_0) and $F_{\mathcal{C}}^L(x, T_0, V_{\mathcal{C}}^L)$ is the Helmholtz free energy. $V_{\mathcal{C}}^L(x, T_0, P_0)$ is calculated from independent *NPT* simulations. The Helmholtz free energy can be computed via the TI calculation. We employ the Uhlenbeck-Ford (UF) model as the liquid reference system, which has been shown to allow accurate free-energy calculations of liquid and is not hampered by the possibility of a liquid-vapor transition as in the case of an ideal gas [7–10].

The Helmholtz free energy $F_{\mathcal{C}}^L(x, T_0, V_{\mathcal{C}}^L)$ of liquid was computed by

$$F_{\mathcal{C}}^L(x, T_0, V_{\mathcal{C}}^L) = F_{\mathcal{C}}^{UF}(x, T_0, V_{\mathcal{C}}^L) + F_{\mathcal{C}}^{IG}(x, T_0, V_{\mathcal{C}}^L) + F_{\mathcal{C}}^{TI}(x, T_0, V_{\mathcal{C}}^L), \quad (\text{S8})$$

where $F_{\mathcal{C}}^{UF}(x, T_0, V_{\mathcal{C}}^L)$ and $F_{\mathcal{C}}^{IG}(x, T_0, V_{\mathcal{C}}^L)$ are the Helmholtz free energy of the UF model and ideal gas, respectively. We eliminated the systematic error by combining the results of the forward and backward processes [11]. The thermodynamic integration term is calculated as

$$F_{\mathcal{C}}^{TI}(x, T_0, V_{\mathcal{C}}^L) = \frac{1}{2} \left[\int_0^1 \langle U_{EAM} - U_{UFM} \rangle_{\lambda, \text{forward}} d\lambda - \int_1^0 \langle U_{EAM} - U_{UFM} \rangle_{\lambda, \text{backward}} d\lambda \right]. \quad (\text{S9})$$

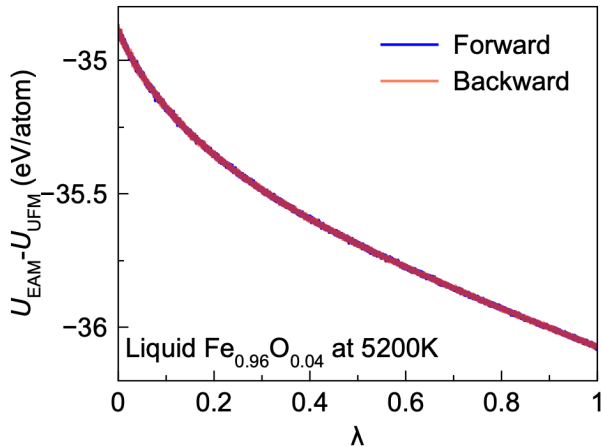


FIG. S5 Nonequilibrium free-energy calculations were performed for liquid $\text{Fe}_{0.96}\text{O}_{0.04}$ at 5200 K using the UF model as reference systems [11].

The detailed derivations for this method are shown in references [7,11]. With 32,000 atoms and 500 *ps* TI simulation, the path between the UF model and $\text{Fe}_{1-x}\text{O}_x$ liquid solutions is sufficiently

smooth, as illustrated in Fig. S5. Similar calculations were carried out for liquid compositions at different temperatures ($x_C^L = 0\%, 4\%, 8\%, 12\%, 16\%, 20\%$; $T = 4600$ K, 4800 K, 5000 K, 5200 K, 5400 K, 5600 K, 5800 K, 6000 K).

Supplementary Note 4 | Redlich-Kister model for superionic state

The Redlich–Kister (RK) expansion is a polynomial form used to account for the non-ideal contributions to the free energy of solutions [12]. As our study involves both liquid and superionic solutions, we adopt a consistent RK formulation of $\text{Fe}_{1-x}\text{O}_x$ for both cases. In this section, we explore the difference between the $\text{Fe}_{1-x}\text{O}_x$ and FeO_x formulations on the fitting of the Gibbs free energy for superionic solution.

Physically, there is no well-defined sublattice to describe the oxygen sites in the superionic state. A plausible model is to assume that oxygen atoms diffuse among the interstitial sublattice of the Fe crystal. In this sense, oxygen atoms can be considered to mix with vacancies, and the chemical composition can be written as $\text{Fe}(\text{V}_{1-y}\text{O}_y)_m$, where V represents vacancies at interstitial sites and m is the number of interstitial sites per Fe atom. Because superionic atoms do not vibrate strictly at well-defined interstitial positions, it is difficult to assign a precise value to m . Thus, m can be treated as an empirical parameter, varying between hcp and bcc structures. For a phase with a single sublattice [13], the Gibbs free energy of $\text{Fe}(\text{V}_{1-y}\text{O}_y)_m$ can be expressed as:

$$G(y) = (1 - y)G_{FeV}^* + yG_{FeO}^* + y(1 - y)\sum_{n=0}(1 - 2y)^nL_n + mk_B T[y \ln y + (1 - y) \ln(1 - y)], \quad (\text{S10})$$

where G_{FeV}^* denotes the Gibbs free energy of the end member FeV_m , which corresponds to the free energy of pure iron G^{Fe} . G_{FeO}^* denotes the free energy of the hypothetical endmember FeO_m , in which all m interstitial sites are fully occupied by oxygen atoms. Thus, $G(y)$ represents the Gibbs free energy of $\text{Fe}(\text{V}_{1-y}\text{O}_y)_m$ per formula unit of FeO_{ym} . We take zero-order term of L_n and express the per-atom Gibbs free energy as

$$G^{SI}(y) = \frac{1}{1+my}\{(1 - y)G^{Fe} + yG^* + y(1 - y)L_0 + mk_B T[y \ln y + (1 - y) \ln(1 - y)]\}. \quad (\text{S11})$$

Both G^* and L_0 are fitting parameters. Defining $z = y \times m$, the chemical formula becomes FeO_z . The Gibbs free energy can then be written as:

$$G^{SI}(z) = G^{Fe} + \left[\frac{z}{m(1+z)}G^* - \frac{z(1+m)}{m(1+z)}G^{Fe} \right] + \frac{z(m-z)}{m^2(1+z)}L_0 + \frac{1}{1+z}k_B T[z \ln z + (m - z) \ln(m - z) - m \ln m]. \quad (\text{S12})$$

FeO_z is equivalent to $\text{Fe}_{1-x}\text{O}_x$ if $x = \frac{z}{1+z}$. Thus, the Gibbs free energy can be further written as:

$$G^{SI}(x) = G^{Fe} + \left(\frac{G^*}{m} - \frac{m+1}{m} G^{Fe} \right) x + \frac{[m(1-x) - x]}{m^2(1-x)^2} L_0 x(1-x) \\ + k_B T \{ x \ln x + [(1-x)m - x] \ln[(1-x)m - x] - m(1-x) \ln m(1-x) \}. \quad (\text{S13})$$

We now evaluate the performance of Eqn. (S13) in comparison with Eqn. (2) of the main text for fitting the free energy data. As shown in Fig. S6(a) and (b), both expressions yield essentially equivalent fits. The equivalence in fitting accuracy can be understood numerically by performing a Taylor expansion. Here, x is a small quantity (~ 0.02), while the order of magnitude of m is on the order of unity. We perform Taylor expansions for terms in Eqn. (S13) with

$$(1-x)^{-1} = 1 + x + x^2 + \dots, \quad \ln m(1-x) = \ln m + \ln(1-x) = \ln m - x - \frac{x^2}{2} - \dots,$$

$$\ln[(1-x)m - x] = \ln m + \ln \left(1 - \frac{m+1}{m} x \right) = \ln m - \frac{m+1}{m} x - \frac{1}{2} \left(\frac{m+1}{m} x \right)^2 - \dots$$

Retaining terms up to 2nd order in x , Eqn. (S13) can be simplified as:

$$G^{SI}(x) = G^{Fe} + Ax + Bx(1-x) + k_B T[x \ln x - x(1-x)], \quad (\text{S14})$$

where $A = \frac{G^*}{m} - \frac{m+1}{m} G^{Fe} - k_B T \ln m + \frac{L_0}{m} - B$, $B = -\frac{m+1}{m} k_B T + \frac{L_0}{m^2}$. We can also perform a

Taylor expansion $\ln(1-x) \approx -x$ for Eqn. (2) to obtain:

$$G(x) = G^{Fe} + ax + x(1-x)L_0 + k_B T[x \ln x - x(1-x)]. \quad (\text{S15})$$

Thus, Eqns. (S14) and (S15) share an identical mathematical form. Consequently, fitting with either the substitutional or sublattice model yields numerically equivalent performance.

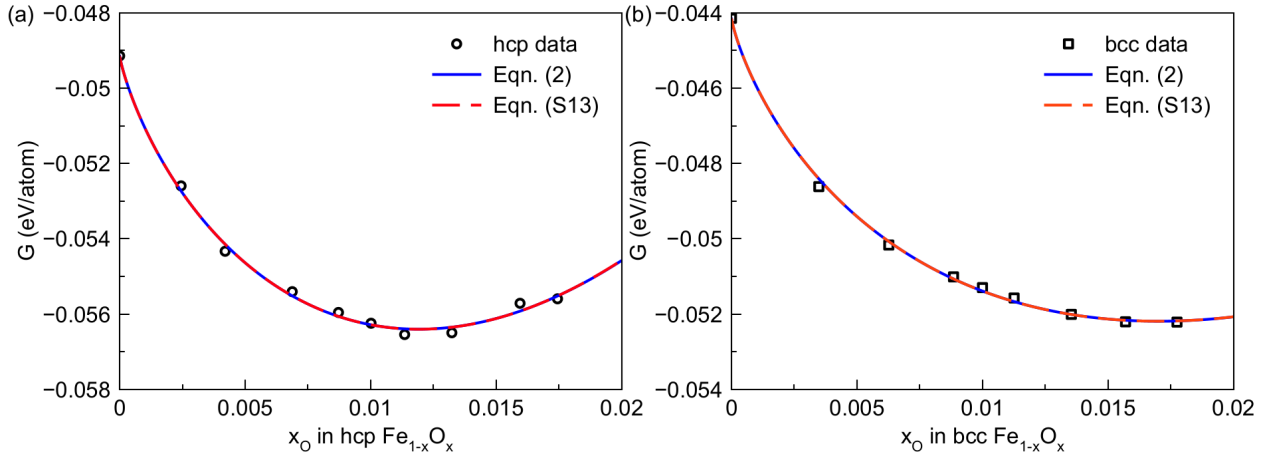


Fig. S6 Relative Gibbs free energy for (a) superionic hcp phases and (b) superionic bcc phases based on different solution formulation, . The free energy data of liquid at 0% and 20% are used as reference.

Supplementary Note 5 | CATI simulation using two different EAM potential

In thermodynamic integration calculations, it is not critical for the reference state to be close in energy to the real state. What matters is that the reference state can be continuously and smoothly connected to the real state without encountering a first-order phase transition along the TI path [14]. To illustrate the minimal impact of the EAM potential on the accuracy of CATI, we use both the EAM potential developed by Davies et al. [5] and the EAM potential from this work as reference states in CATI simulations to compute the *ab initio* Gibbs free energy of Fe₂₀₀O₅₀ liquid at 323 GPa and 5500 K, which can be well simulated by both potentials. The TI paths originating from the two potentials are shown in Fig. S7(a). Based on Eqn. (4) in the main text, $G_A = G_C + f_{PV} + f_{TI}$, where $f_{PV} = P(V_A - V_C) - \int_{V_C}^{V_A} P_C(V)dV$, and $f_{TI} = \int_0^1 \langle U_A - U_C \rangle_{\lambda, V_A} d\lambda$. Figure S7(b) shows the relevant values for both potentials. The Gibbs free energy G_C differs significantly between the two EAM potentials. This difference is then corrected by the f_{TI} and f_{PV} terms. The f_{TI} term provides the main contribution, while f_{PV} contributes only marginally. Despite the difference in reference potentials, the final *ab initio* Gibbs free energy G_A obtained from CATI calculations is nearly identical, with a discrepancy of only ~0.9 meV/atom, which is within the statistical error.

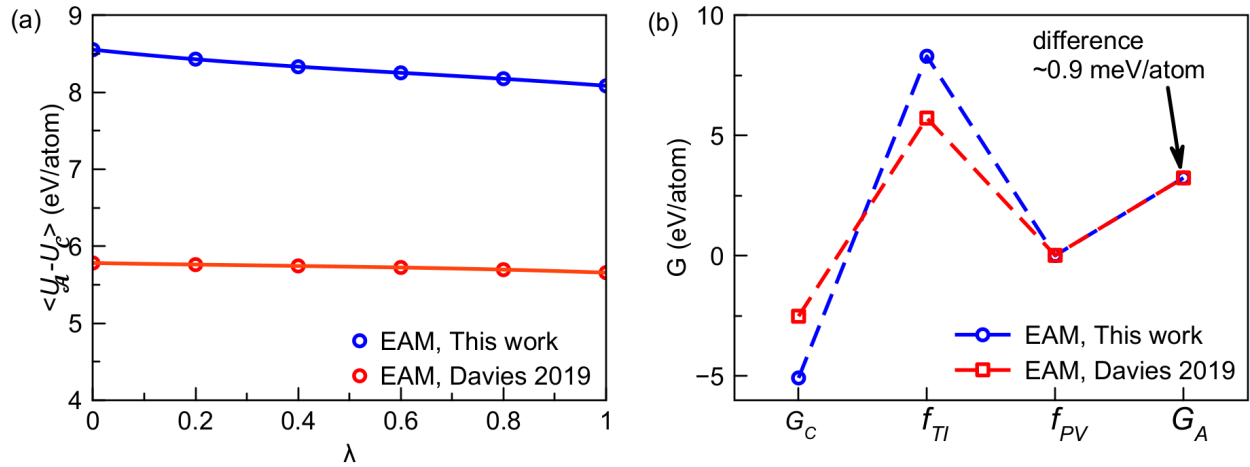


Fig. S7 CATI calculation for Fe₂₀₀O₅₀ liquid at 323 GPa and 5500 K using two EAM potentials as the reference state. (a) The TI path from the classical to the *ab initio* system. (b) The free energy contribution in CATI calculation from Eqn. (4).

Supplementary Note 6 | Uncertainties in the phase diagram

The uncertainties in the *ab initio* phase diagram obtained by our method primarily arise from three sources: (1) the superionic-liquid coexistence simulations that result in (x_C^L, x_C^{SI}) , leading to δ_x ; (2) the error from the fitting with Redlich-Kister model; (3) classical-to-*ab initio* thermodynamic integration (CATI) calculations. (1) and (2) leads to errors in classical Gibbs free energy (δ_{G_C}). (3) involves the uncertainties from first-principles calculations which leads to δ_{TI} and δ_{PV} . These errors finally cause uncertainties in G_A and phase diagram. Below, we analyze how these errors propagate to the uncertainties in the final phase diagram.

(1) System size in superionic-liquid coexistence simulations.

In our superionic-liquid coexistence simulations, a cell of $105.7 \text{ \AA} \times 29.7 \text{ \AA} \times 27.9 \text{ \AA}$ containing over 12,846 atoms was used to determine x_C^{SI} and x_C^L in Eqn. (1). To evaluate the size effect, we constructed a series of models with sizes $L \times 29.7 \text{ \AA} \times 27.9 \text{ \AA}$, where L ranges from 52.9 \AA to 527.9 \AA in Fig. S8(a). Using the results from the 527.9 \AA model as a reference, the 105.7 \AA model yields an uncertainty of $\delta_x \sim 0.1$ at.% in the value of $x_C^L - x_C^{SI}$. In Eqn. (1), $G_C^{SI}(x_{C0}^{SI}, T_0) = G_C^L(x_{C0}^L, T_0) - (x_{C0}^L - x_{C0}^{SI}) \frac{\partial G_C^L(x)}{\partial x} \Big|_{x=x_{C0}^L}$. The error of $G_C^L(x_{C0}^L, T_0)$, $\delta_{G_C^L}$, was estimated to be 0.04 meV/atom, based on three independent TI simulations. The standard deviation

of $G_C^{SI}(x_{C0}^{SI}, T_0)$, $\delta_{G_C^{SI}}$, was calculated by $\delta_{G_C^{SI}} = \sqrt{\delta_x^2 \left(\frac{\partial G_C^L(x_{C0}^L)}{\partial x} \right)^2 + \delta_{G_C^L}^2}$. At 5500 K , $\frac{\partial G_C^L(x_{C0}^L)}{\partial x} = -2.3963 \text{ eV/atom}$. These lead to an uncertainty of ~ 2.4 meV/atom for $G_C^{SI}(x_{C0}^{SI}, T_0)$.

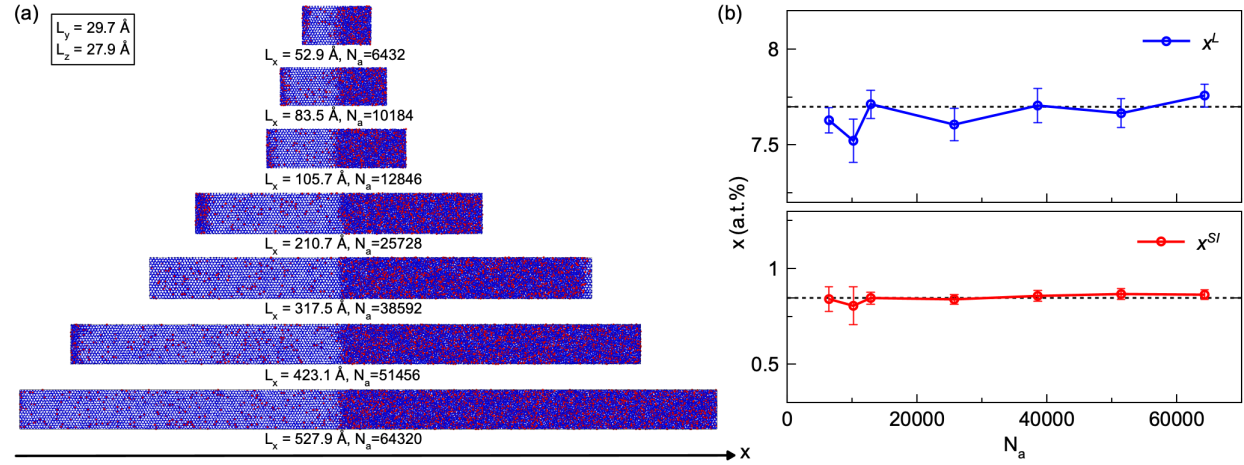


Fig. S8 Size effect on the superionic–liquid coexistence simulation. (a) Simulation models with varying lengths perpendicular to the interface. (b) Solidus (x^{SI}) and liquidus (x^L) at 5500 K

obtained using different simulation sizes. Error bars represent the standard deviation from three independent simulations. The dashed line indicates the system size used in the thermodynamic calculations presented in the main text.

(2) Fitting error with Redlich-Kister model

To evaluate the error introduced by the RK fitting, we present the difference between the RK-fitted results and the original data in Fig. S9. For the EAM results, the fitting errors for the liquid, superionic hcp, and superionic bcc phases are 0.02 meV/atom, 0.13 meV/atom, and 0.09 meV/atom, respectively. For the DFT results, the fitting errors for the liquid, superionic hcp, and superionic bcc phases are 0.2 meV/atom, 0.7 meV/atom, and 0.2 meV/atom, respectively.

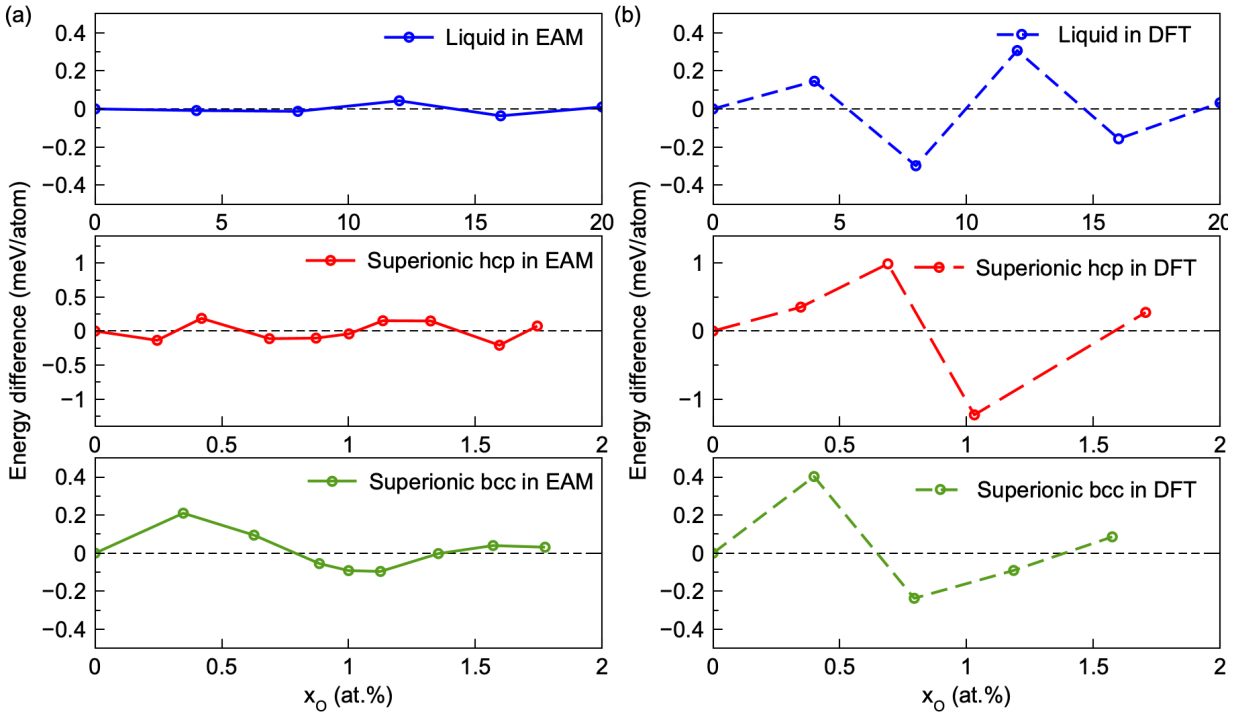


Fig. S9 Energy difference between the calculated data and the fitted data by Redlich-Kister free-energy model for (a) EAM and (b) DFT at 5500 K and 323 GPa.

(3) Size effect in CATI simulations.

To assess the finite-size effect on the free energy in CATI simulations, we tested several system sizes for the pure bcc Fe phase. Specifically, the Helmholtz free energy at 5500 K and ~ 323 GPa was computed for systems containing 128, 250, 432, and 686 atoms. The resulting values as a function of system size are shown in Fig. S10. The free energy difference between the 250-atom

and 686-atom systems is only 0.6 meV/atom, confirming that finite-size effects are very small. Based on this analysis, we assign $\delta_{TI} = 0.6$ meV/atom for the liquid, superionic hcp, and superionic bcc phases, without accounting for error cancellation in the relative free energy calculations.

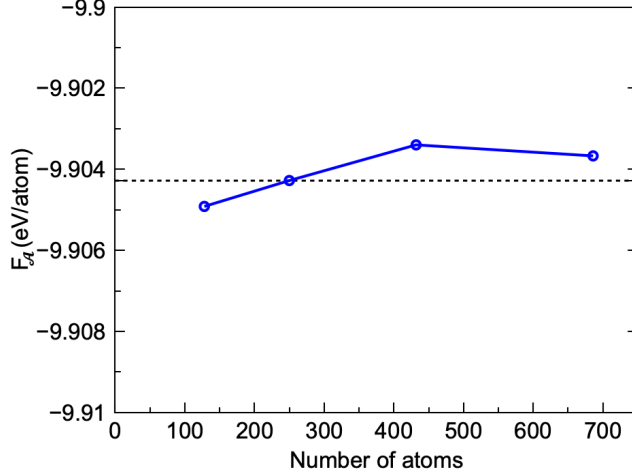


Fig. S10 Helmholtz free energies computed for the bcc Fe phase at 5500 K and a density of 13.314 g/cm³ (~323 GPa) using different system sizes. The dashed line indicates the value used in the main text.

Based on the above analysis, the uncertainties in G_c and f_{TI} , i.e., $\delta_{G_c^{SI}}$, $\delta_{G_c^L}$, and δ_{TI} , are 2.4 meV/atom, 0.04 meV/atom, and 0.6 meV/atom, respectively. As $G_A = G_c + f_{PV} + f_{TI}$, we also need to determine the uncertainty in the f_{PV} term. This term is expressed as $f_{PV} = PV_A - PV_c - \int_{V_c}^{V_A} P_c(V)dV$. To obtain PV_A and PV_c , we performed three independent NVT runs at volumes corresponding to ~323 GPa and 5500 K using both classical MD and AIMD simulations. These provide δ_{PV_c} of 0.0001 meV/atom and δ_{PV_A} of 4 meV/atom. The fact that δ_{PV_c} is much smaller than δ_{PV_A} is due to significant larger size in the classical MD simulations. The uncertainty in PV_A is similar to the difference between the PAW16 potential and all-electron calculations, as shown in Fig. R12(c). We can now compute the standard error propagation to f_{PV} as $\delta_{PV} = \sqrt{\left[\frac{\partial f_{PV}}{\partial(PV_A)}\right]^2(\delta_{PV_A})^2 + \left[\frac{\partial f_{PV}}{\partial(PV_c)}\right]^2(\delta_{PV_c})^2} = 0.2$ meV/atom. Now the uncertainty in G_A can be calculated by $\delta_{G_A} = \sqrt{(\delta_{G_c})^2 + (\delta_{PV})^2 + (\delta_{TI})^2}$. The resulting uncertainties in G_A^L and G_A^{SI} are 0.6 meV/atom and 2.5 meV/atom, respectively. The values of x^{SI} and x^L are obtained

by solving the Eqn. (A6) of the main text. Given the uncertainties in $G_{\mathcal{A}}^L$ and $G_{\mathcal{A}}^{SI}$, we obtained $x^L=14.8\pm0.4$ at.% and $x^{SI}=0.47\pm0.01$ at.% at 5500 K. The uncertainty in $D^{s/l}$ can be estimated using $\sigma_{D^{s/l}} = D^{s/l} \sqrt{\left(\frac{\sigma_{x^{SI}}}{x^{SI}}\right)^2 + \left(\frac{\sigma_{x^L}}{x^L}\right)^2} = 0.001$. The estimated uncertainty ranges for both the solidus and liquidus lines are shown in Fig. 4(c) of the main text.

Supplementary Note 7 | DFT accuracy

We test the effect of different exchange–correlation functionals and compare PAW16 results with all-electron calculations to assess the accuracy of DFT. We compared the equation of state (EOS) of the Fe-hcp phase with experimental data using three exchange–correlation functionals: PBE [15], PBEsol [16], and SCAN [17]. We computed the EOS at 300 K using the quasi-harmonic approximation (QHA). As shown in Fig. R11, the PBE functional yields results closest to the experimental values, which is consistent with previous study [18]. Thus, we consider the PBE functional a suitable choice for our study.

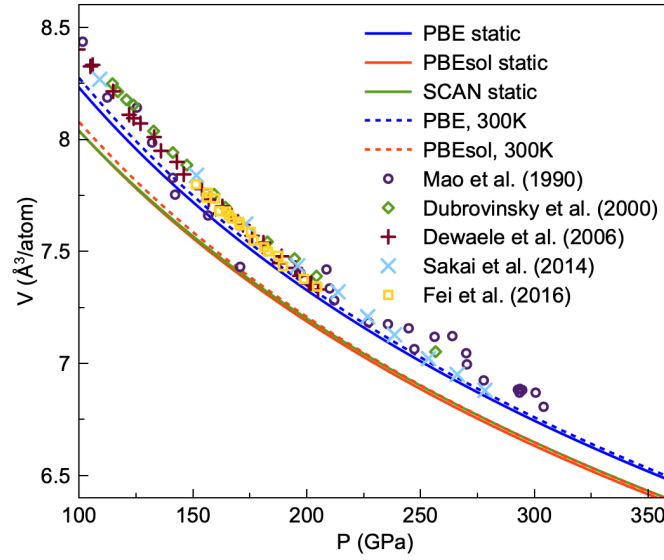


Fig. S11 Comparison between experimental and theoretical equation of state (EoS) of hcp-Fe at 300 K. Symbols were obtained in static compression experiments on a diamond anvil cell (DAC) [19–23]. The solid lines represent results obtained without considering the contribution of vibrational entropy to the free energy, while the dashed lines include the effect of vibrational entropy.

We compared the PAW16 potential with all-electron calculation results. Using the same PBE functional, we calculated the energy E of pure iron in both *hcp* and *bcc* phases at various volumes V , as shown in Fig. S12(a) and (b). The all-electron calculations were performed using the ELK package [24]. The $E-V$ data were fitted with a third-order Birch-Murnaghan equation. The corresponding $P-V$ curves were derived from $P = -\frac{\partial E}{\partial V}$ and shown in Fig. S12(c). The results obtained with the PAW16 potential show good agreement with the all-electron results with a difference of EOS by 0.005-0.01 Å³/atom.

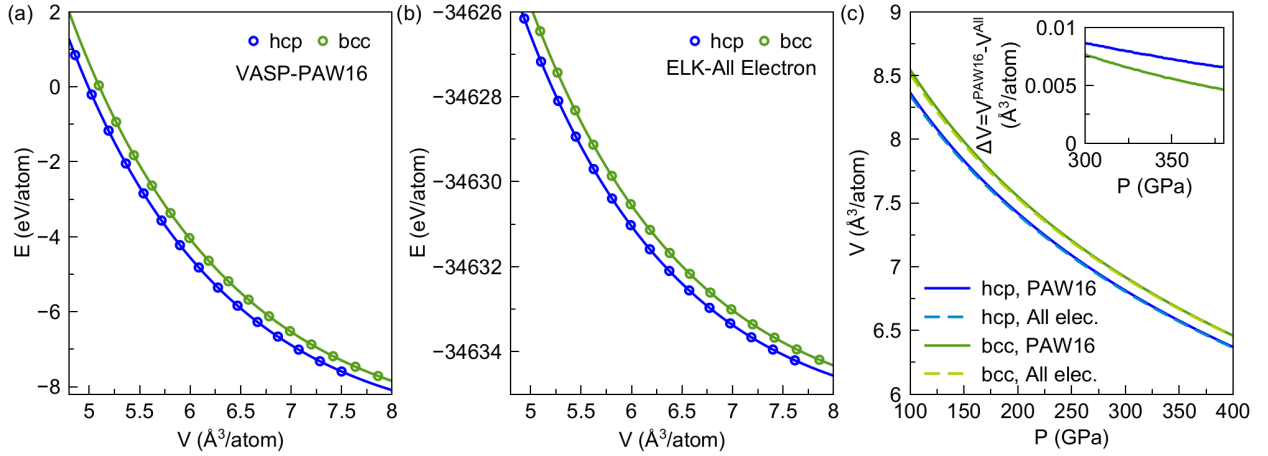


Fig. S12 Energy-volume relationship of pure Fe in the *hcp* and *bcc* phases from static calculations with $T_{elec} = 6000$ K using (a) the VASP-PAW16 pseudopotential and (b) the ELK all-electron method. The solid lines in the top panels represent the third-order Birch-Murnaghan (BM) fitting results, while the bottom panels show the differences between the fitted values and the actual data. (c) Static equation of state of pure Fe with $T_{elec} = 6000$ K. The solid (dashed) line corresponds to results obtained with the VASP-PAW16 pseudopotential (ELK all-electron method). The blue line and green lines represent the *hcp* and *bcc* phases, respectively. The subfigure shows the difference in volume between the VASP and ELK results at corresponding pressure.

Supplementary Note 8 | Phase competition between superionic *hcp* and *bcc*

Based on the Gibbs free energy data, we analyze the contributions to the phase competition between superionic *hcp* and superionic *bcc* phases as a function of oxygen concentrations. The Gibbs free energy is given by $G = U + PV - TS$, where U is the internal energy, PV is the pressure-volume term, and S is the total entropy. For the superionic Fe-O alloy, the entropy S includes contributions from electronic, vibrational, and configurational sources, among others. We

denote the electronic entropy as S_{elec} , which can be directly computed from DFT calculations. Other entropy contributes that are difficult to compute directly are grouped together as S_{excess} . Since we have already computed G , U , PV , and TS_{elec} , we can deduce the remaining entropy contribution from: $-TS_{excess} = G - U - PV + TS_{elec}$. To understand why increasing superionic oxygen stabilizes the bcc phase relative to the hcp phase, we focus on the energy differences between the two phases:

$$\Delta G = G^{bcc} - G^{hcp}, \quad \Delta U = U^{bcc} - U^{hcp}, \quad \Delta(PV) = P(V^{bcc} - V^{hcp}),$$

$$\Delta(-TS_{elec}) = (-TS_{elec}^{bcc}) - (-TS_{elec}^{hcp}), \quad \Delta(-TS_{excess}) = (-TS_{excess}^{bcc}) - (-TS_{excess}^{hcp}).$$

As shown in Fig. S13, the U and PV terms for the bcc phase are larger than those for the hcp phase. However, the entropy of the bcc phase is also larger than that of the hcp phase, such that $S^{bcc} > S^{hcp}$, corresponding to a negative $\Delta(-TS)$. As the oxygen concentration increases, the relative differences in U and PV decrease, suggesting that oxygen reduces the enthalpy difference between bcc and hcp. Meanwhile, the excess entropy of the bcc phase increases significantly, leading to a rapid decrease in $\Delta(-TS_{excess})$. This causes the Gibbs free energy of the bcc phase to become lower than that of the hcp phase when $x_O > 3$ at. %. This behavior can be attributed to the enhancement of cooperative Fe atom motion by superionic oxygen diffusion in the bcc lattice, which increases both the vibrational and configurational entropy of the bcc phase.

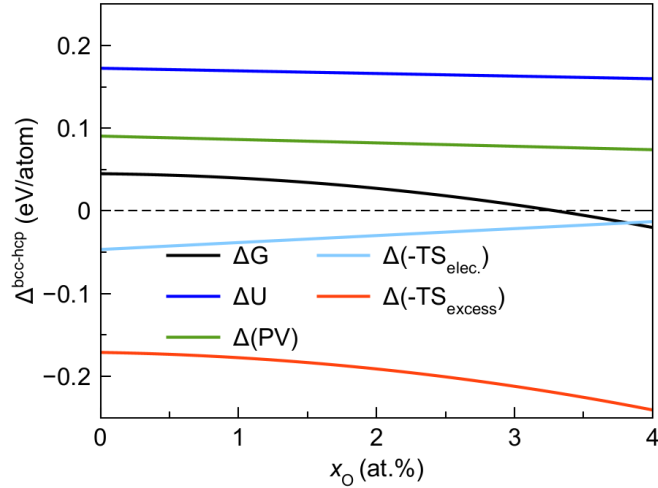


Fig. S13. Contributions to the free energy difference between superionic bcc and hcp phases as a function of oxygen concentration at 5500 K and 323 GPa.

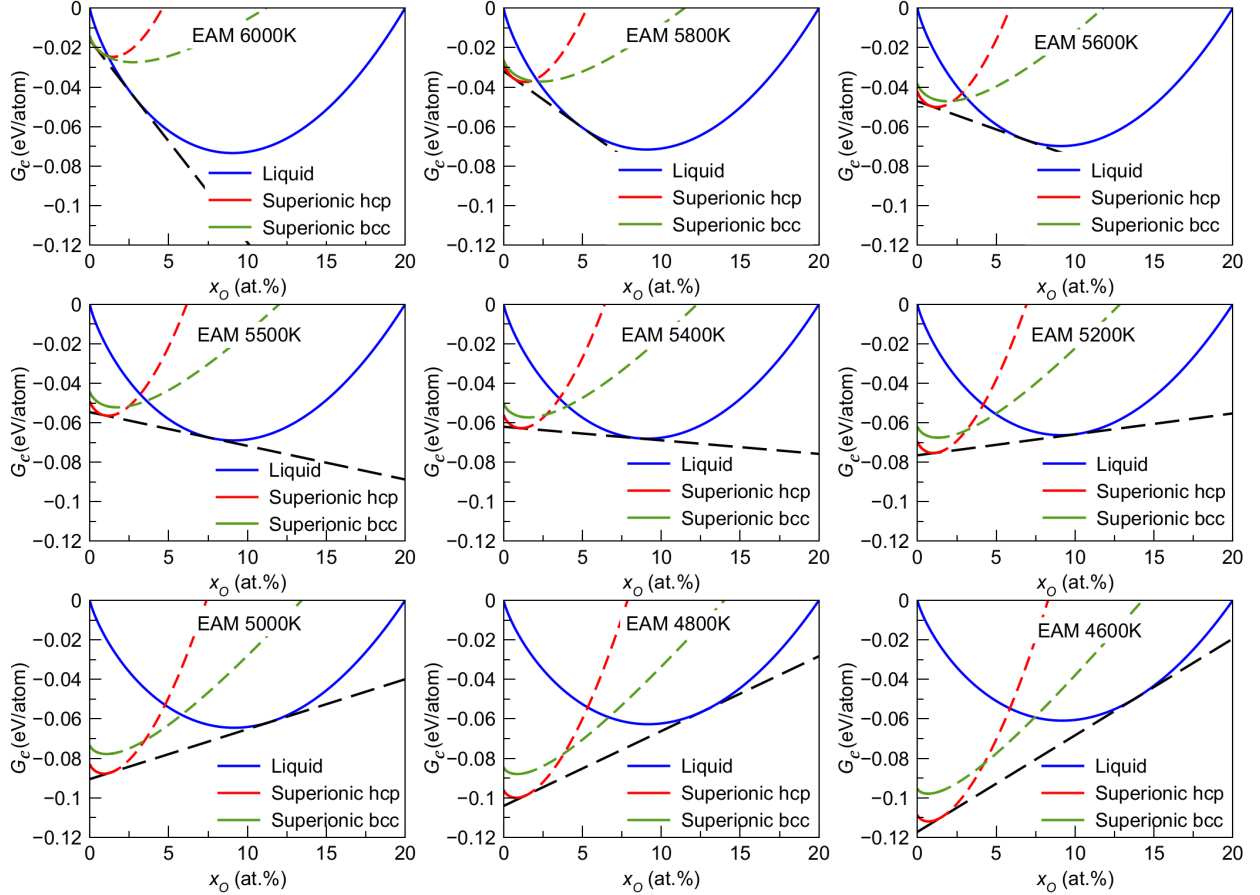


FIG. S14 The relative Gibbs free energy for liquid and superionic solutions $\text{Fe}_{1-x}\text{O}_x$ ranging from 4600 K to 6000 K at 323 GPa from EAM potential. The red/green solid (dashed) line for superionic indicates the interpolation (extrapolated) results using RK expansion (with $n_k = 0$ fitting). The black dashed line is the common tangent line of Gibbs free energy for liquid and superionic hcp, which defines the solidus and liquidus composition.

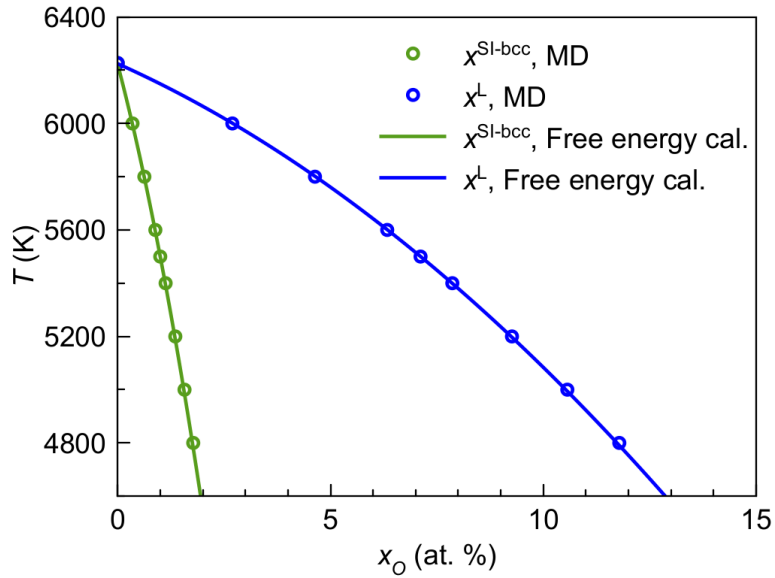


FIG. S15 The phase diagram between superionic bcc and liquid from MD simulation at 323 GPa. The circles are from direct superionic bcc-liquid coexistence simulations. The lines are from free energy calculations.

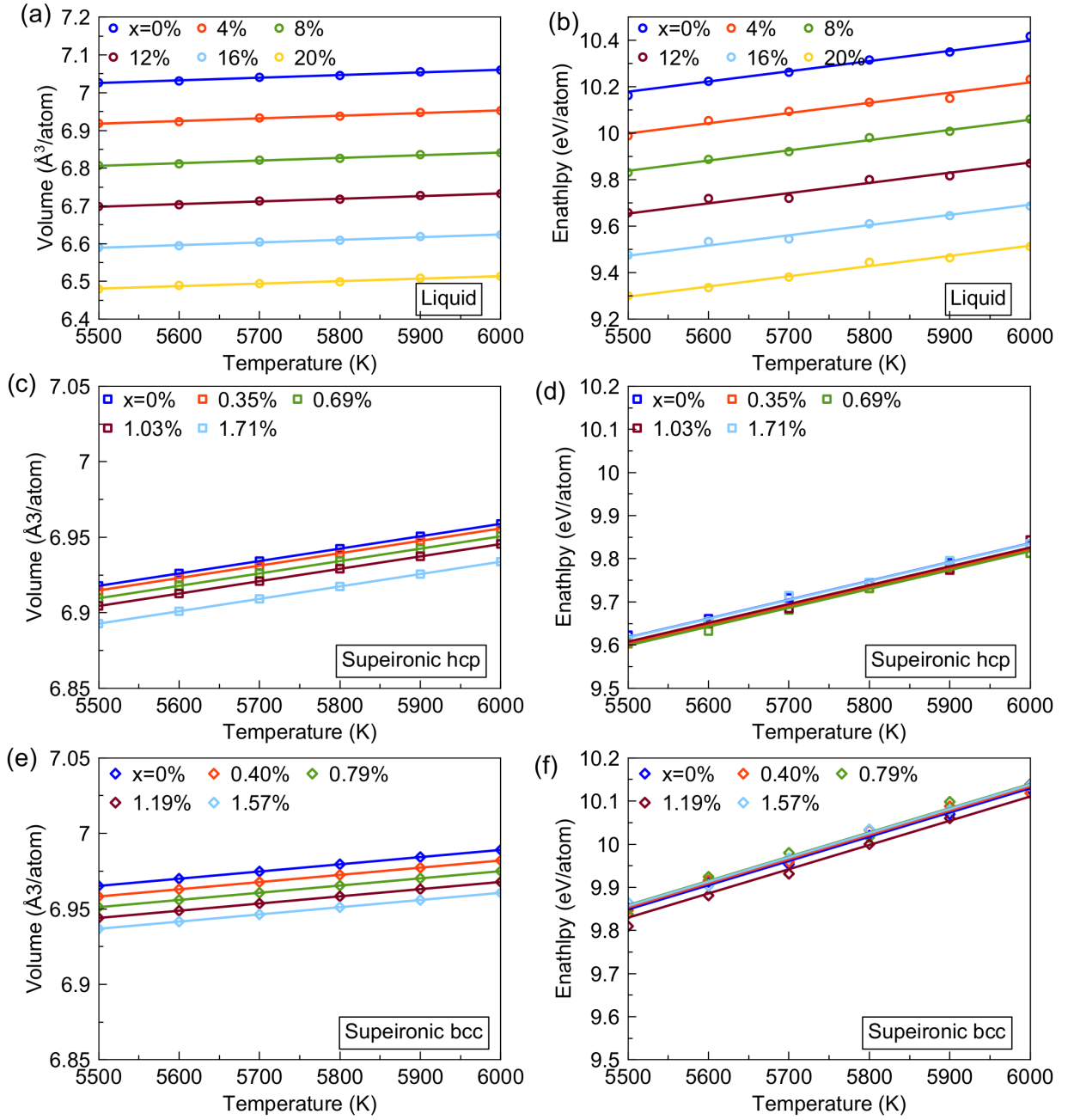


FIG. S16 Volume and Enthalpy for liquid, superionic hcp and superionic bcc $\text{Fe}_{1-x}\text{O}_x$ ranging from 5500 K to 6000 K at 323 GPa with AIMD. The solid lines represent the first-order polynomial fitting.

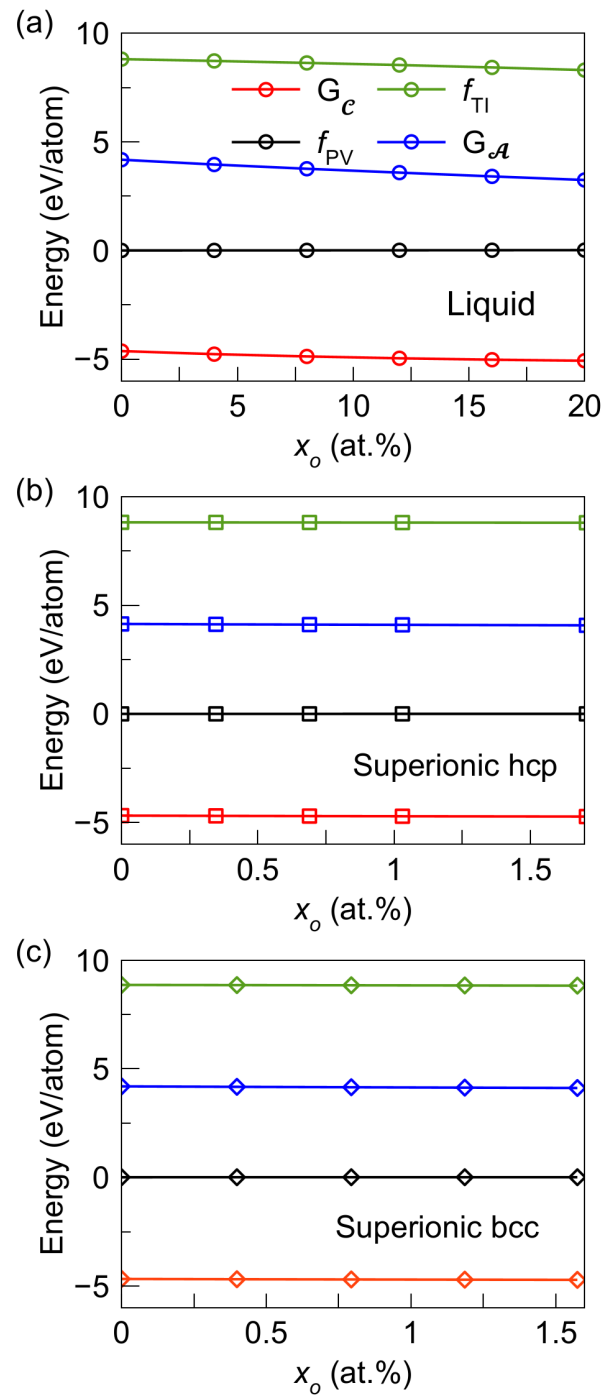


FIG. S17 The effective terms in Gibbs free energy calculation with Eqn. (4) for (a) liquid, (b) superionic hcp and (c) superionic bcc $\text{Fe}_{1-x}\text{O}_x$ at 5500 K and 323 GPa.

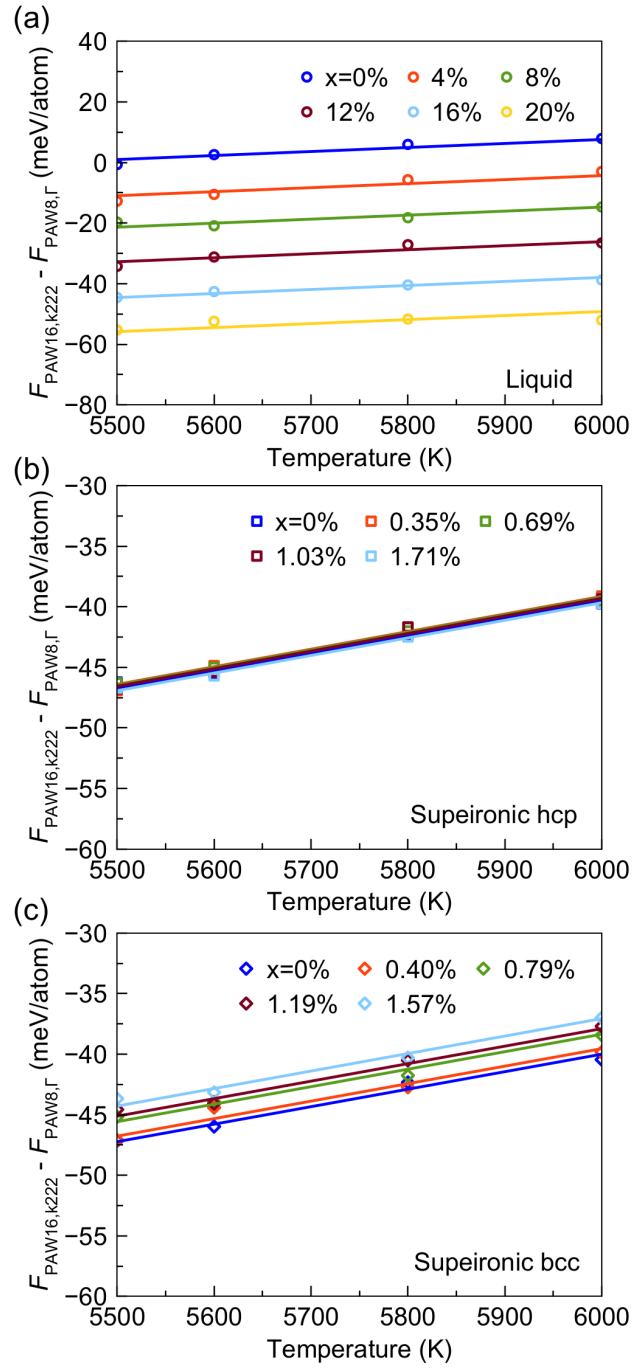


FIG. S18 The FEP calculation results for (a) liquid, (b) superionic hcp and (c) superionic bcc $\text{Fe}_{1-x}\text{O}_x$ at different temperatures. The solid lines represent the first-order polynomial fitting.

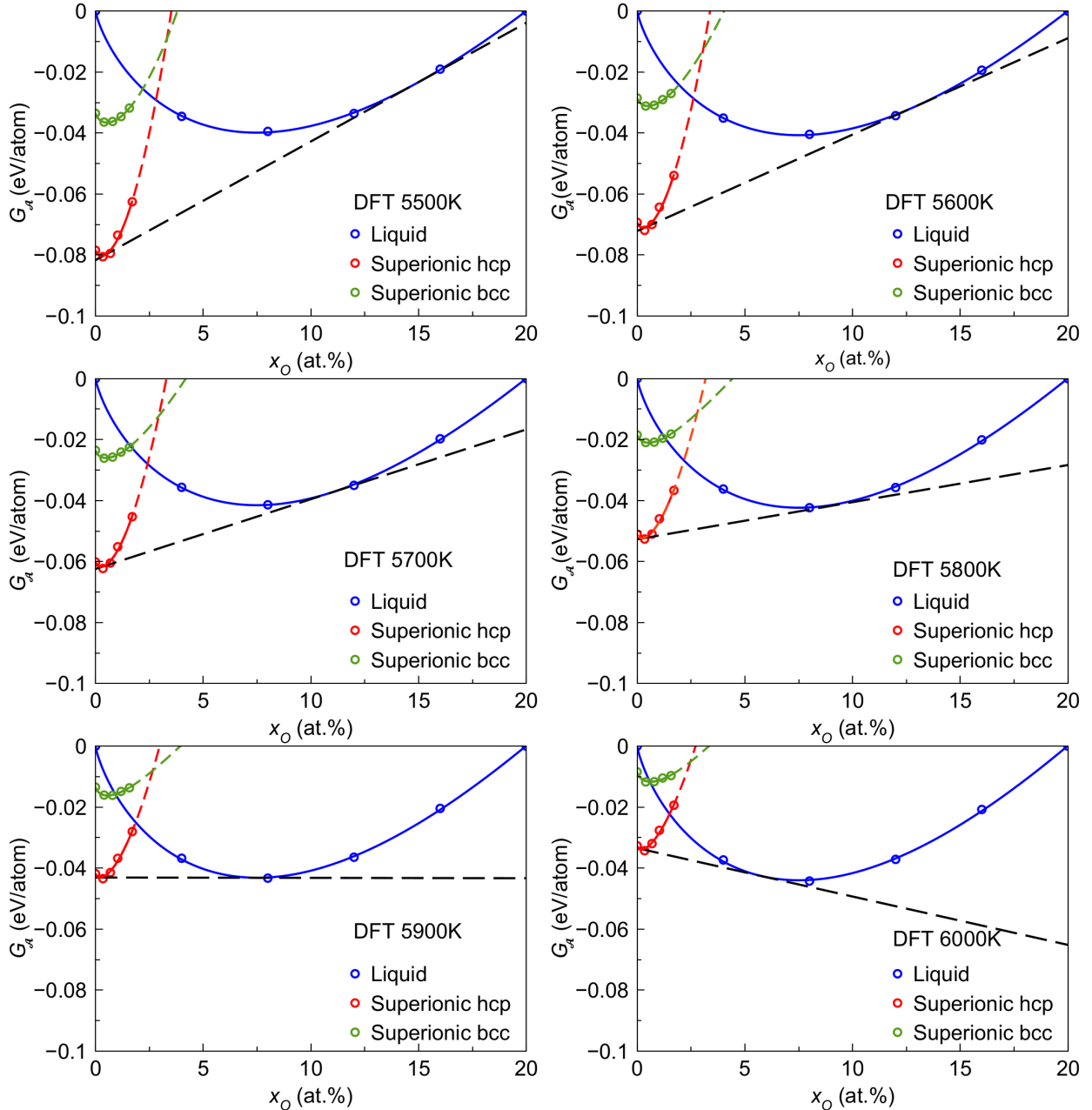


FIG. S19 The *ab initio* relative Gibbs free energy for liquid and superionic solutions $\text{Fe}_{1-x}\text{O}_x$ ranging from 5500 K to 6000 K at 323 GPa. The red/green solid (dashed) lines for superionic indicate the interpolation (extrapolated) results using RK expansion (with $n_k = 0$ fitting). The black dashed line is the standard tangent line of Gibbs free energy for liquid and superionic hcp, defining the solidus and liquidus composition.

Supplementary References

- [1] A. B. Belonoshko, T. Lukinov, J. Fu, J. Zhao, S. Davis, and S. I. Simak, Stabilization of body-centred cubic iron under inner-core conditions, *Nature Geoscience* **10**, 312 (2017).
- [2] M. Ghosh, S. Zhang, L. Hu, and S. Hu, Cooperative diffusion in body-centered cubic iron in Earth and super-Earths' inner core conditions, *Journal of Physics: Condensed Matter* **35**, 154002 (2023).
- [3] Y.-Y. Ye, Y. Chen, K.-M. Ho, B. Harmon, and P.-A. Lindgrd, Phonon-phonon coupling and the stability of the high-temperature bcc phase of Zr, *Physical Review Letters* **58**, 1769 (1987).
- [4] R. M. Wentzcovitch and M. L. Cohen, Theoretical model for the hcp-bcc transition in Mg, *Physical Review B* **37**, 5571 (1988).
- [5] C. J. Davies, M. Pozzo, and D. Alfè, Assessing the inner core nucleation paradox with atomic-scale simulations, *Earth and Planetary Science Letters* **507**, 1 (2019).
- [6] Y. He, S. Sun, D. Y. Kim, B. G. Jang, H. Li, and H. Mao, Superionic iron alloys and their seismic velocities in Earth's inner core, *Nature* **602**, 258 (2022).
- [7] R. Paula Leite, R. Freitas, R. Azevedo, and M. de Koning, The Uhlenbeck-Ford model: Exact virial coefficients and application as a reference system in fluid-phase free-energy calculations, *Journal of Chemical Physics* **145**, 194101 (2016).
- [8] R. Paula Leite, P. A. Santos-Florez, and M. de Koning, Uhlenbeck-Ford model: Phase diagram and corresponding-states analysis, *Physical Review E* **96**, 032115 (2017).
- [9] S. Cajahuaranga and A. Antonelli, Nonequilibrium free energy methods applied to magnetic systems: The degenerate Ising model, *Journal of Statistical Physics* **175**, 1006 (2019).
- [10] S. Menon, Y. Lysogorskiy, J. Rogal, and R. Drautz, Automated free-energy calculation from atomistic simulations, *Physical Review Materials* **5**, 103801 (2021).
- [11] R. Paula Leite and M. de Koning, Nonequilibrium free-energy calculations of fluids using LAMMPS, *Computational Materials Science* **159**, 316 (2019).
- [12] O. Redlich and A. Kister, Algebraic representation of thermodynamic properties and the classification of solutions, *Industrial & Engineering Chemistry* **40**, 345 (1948).

- [13] Z.-K. Liu, Computational thermodynamics and its applications, *Acta Materialia* **200**, 745 (2020).
- [14] C. Vega, E. Sanz, J. Abascal, and E. Noya, Determination of phase diagrams via computer simulation: methodology and applications to water, electrolytes and proteins, *Journal of Physics: Condensed Matter* **20**, 153101 (2008).
- [15] J. P. Perdew, K. Burke, and M. Ernzerhof, Generalized gradient approximation made simple, *Physical Review Letters* **77**, 3865 (1996).
- [16] J. P. Perdew, A. Ruzsinszky, G. I. Csonka, O. A. Vydrov, G. E. Scuseria, L. A. Constantin, X. Zhou, and K. Burke, Restoring the density-gradient expansion for exchange in solids and surfaces, *Physical Review Letters* **100**, 136406 (2008).
- [17] J. Sun, A. Ruzsinszky, and J. P. Perdew, Strongly constrained and appropriately normed semilocal density functional, *Physical Review Letters* **115**, 036402 (2015).
- [18] J. Zhuang, H. Wang, Q. Zhang, and R. M. Wentzcovitch, Thermodynamic properties of ϵ -Fe with thermal electronic excitation effects on vibrational spectra, *Physical Review B* **103**, 144102 (2021).
- [19] A. Dewaele, P. Loubeyre, F. Occelli, M. Mezouar, P. I. Dorogokupets, and M. Torrent, Quasihydrostatic equation of state of iron above 2 Mbar, *Physical Review Letters* **97**, 215504 (2006).
- [20] H. Mao, Y. Wu, L. Chen, J. Shu, and A. P. Jephcoat, Static compression of iron to 300 GPa and Fe_{0.8}Ni_{0.2} alloy to 260 GPa: Implications for composition of the core, *Journal of Geophysical Research: Solid Earth* **95**, 21737 (1990).
- [21] L. Dubrovinsky, S. Saxena, F. Tutti, S. Rekhi, and T. LeBehan, In situ X-ray study of thermal expansion and phase transition of iron at multimegabar pressure, *Physical Review Letters* **84**, 1720 (2000).
- [22] T. Sakai, S. Takahashi, N. Nishitani, I. Mashino, E. Ohtani, and N. Hirao, Equation of state of pure iron and Fe_{0.9}Ni_{0.1} alloy up to 3 Mbar, *Physics of the Earth and Planetary Interiors* **228**, 114 (2014).

[23] Y. Fei, C. Murphy, Y. Shibasaki, A. Shahar, and H. Huang, Thermal equation of state of hcp-iron: Constraint on the density deficit of Earth's solid inner core, *Geophysical Research Letters* **43**, 6837 (2016).

[24] The ELK code, <http://elk.sourceforge.net>